AIMS Mathematics, 11(11): 37686–37734.
DOI: 10.3934/math.20261458
Received: 16 June 2026
Revised: 28 September 2026
Accepted: 08 October 2026
Published: 13 November 2026

https://www.aimspress.com/journal/Math

Research article

Julia and Mandelbrot set-based fractal transformations applied to a 4D memristive chaotic system without equilibria

Michael I. Kopp[1] **and Inna Samuilik**[2,3,*]

[1] Institute for Single Crystals, NAS Ukraine, Nauky Ave. 60, Kharkiv 61072, Ukraine
[2] Institute of Life Sciences and Technologies, Daugavpils University, 13 Vienibas Street, LV-5401 Daugavpils, Latvia
[3] Institute of Applied Mathematics, Riga Technical University, LV-1048 Riga, Latvia

* **Correspondence:** Email: inna.samuilika@rtu.lv.

Abstract: This paper presents a detailed dynamical analysis of a four-dimensional (4D) memristive chaotic system without equilibria and studies fractal transformations of its attractor as a geometric post-processing tool. The chaotic nature of the system was confirmed through the Lyapunov exponent spectrum, computed with an explicit statistical criterion for vanishing exponents, phase portraits, multistability, and offset boosting analysis. A Lyapunov-function analysis and long-time simulations characterized the boundedness of trajectories. Poincaré cross-sections and broadband spectral analysis revealed the rich geometric structure of the hidden attractors, and NIST SP 800-22 randomness tests validated the statistical quality of the generated sequences. Electronic circuit implementation validated the theoretical model using Multisim simulations. We applied inverse Julia map-based binary and ternary algorithms to phase space projections of the system, demonstrating systematic structural multiplication: after N iterations, the transformed set consisted of 2^N congruent copies of the original structure with exact 2^N-fold rotational symmetry, which was proved analytically. The ternary extension operates in three-dimensional phase space and was formulated under two distinct hypercomplex multiplication rules, which are shown to yield fundamentally different geometric outcomes: anisotropic ribbon-like structures in one case and isotropic concentric configurations in the other. We introduced three novel Mandelbrot-based fractal transformation methods: the Mandelbrot orbit cloud, the Mandelbrot multiscroll expansion, and the fractal web. The work was a dynamical and geometric study; engineering applications of the transformed attractors are not considered here and are left for future work.

Keywords: memristor; chaotic system; dynamical analysis; circuit implementation; fractal transformation; Julia set; Mandelbrot set
Mathematics Subject Classification: 34C28, 37D45, 28A80, 37F10, 94C05

1. Introduction

The intersection of chaos theory and fractal geometry has remained an active and productive research domain for several decades. Chaotic dynamical systems generate complex trajectories exhibiting sensitivity to initial conditions, whereas fractal constructions produce self-similar geometries through iterative nonlinear mappings [1–3]. The integration of these paradigms enables systematic transformation of chaotic attractors into geometrically enriched structures while preserving their essential dynamical properties.

Following Chua's theoretical prediction of the memristor [4] and its experimental realization [5], memristive nonlinear systems have become a central topic in modern chaos research. In particular, systems possessing hidden attractors, which are attractors not associated with unstable equilibria, have attracted considerable attention due to their nontrivial basin structure and analytical complexity. Memristive chaotic and hyperchaotic systems without equilibrium points represent an especially challenging and interesting class, since their dynamics cannot be inferred from local linearization and require global analysis.

Notable developments include chaotic systems without equilibria [6], 4D memristor-based hyperchaotic models with circuit realization [7], parameter-dependent equilibrium structures [8], and configurations exhibiting hidden chaos together with offset boosting phenomena [9]. Multistability and antimonotonicity in hidden attractor systems were systematically examined in [10], while multi-wing behavior in memristor-based systems without equilibria was reported in [11]. These studies demonstrate that architecturally simple nonlinear models can exhibit rich global dynamics. Recent investigations have shown that hyperchaotic behavior may arise in compact four-dimensional systems containing only a small number of algebraic terms. In [12], a seven-term 4D model without equilibrium states was introduced and its chaotic properties were established through Lyapunov analysis. Subsequent works [13, 14] incorporated memristive elements, yielding hyperchaotic regimes characterized by two positive Lyapunov exponents and elevated Kaplan–Yorke dimensions. Further developments [15] addressed hidden attractors, adaptive coupling mechanisms, and hardware-oriented realizations. These results motivate continued exploration of structurally simple yet dynamically rich memristive chaotic systems.

Parallel to the development of new chaotic generators, fractal transformation techniques have emerged as an effective tool for structural modification of attractors. Classical multi-scroll generation methods often rely on piecewise-linear functions [16, 17], discontinuous switching mechanisms [18, 19], or trigonometric nonlinearities [20, 21]. Although effective, such approaches frequently introduce non-differentiabilities that complicate theoretical analysis and practical implementation.

In recent years, multi-scroll generation methods have developed rapidly, and memristors are increasingly used as the scroll-generating element itself. Wan et al. [22] introduced a memristive autapse into a neuron model and obtained a multiscroll hidden attractor whose number of scrolls is controlled by the memristor, with an application to image encryption. A robust full-parameter control method for constructing multiscroll Hopfield neural networks via a memristor was proposed in [23], and a state-based nonlinear mapping method for constructing a conservative oscillator that generates a cellular chaotic sea, together with its hardware implementation, was developed in [24]. In all of these approaches, the multi-scroll structure is produced by modifying the vector field of the dynamical system. The fractal transformations considered in the present work follow a different route: They act

on the generated trajectory and leave the underlying dynamics unchanged.

An alternative paradigm integrates dynamical systems with fractal geometry via inverse Julia transformations. Originating from Julia's early work on complex quadratic maps [25] and later formalized in dynamical applications, this approach constructs structural multiplication through iterative inverse polynomial operations. Bouallegue et al. [26] introduced the concept of applying reverse Julia mappings to chaotic sequences, establishing a "fractal process" for generating multi-scroll and multi-wing attractors. Their binary scheme employs inverse square-root operations applied to planar chaotic projections, enabling controlled geometric replication through successive iterations. The method was subsequently validated for various classical chaotic systems [27, 28].

A systematic mathematical formulation of binary and ternary fractal algorithms was provided by Dai et al. [29], who demonstrated that structural multiplication follows a power-law relation, with the number of structures doubling at each iteration. Their analysis established that fractal transformations preserve key dynamical invariants, including positive Lyapunov exponents, while significantly reorganizing the geometric structure. Extensions of fractal-transformed chaotic systems have found applications in secure communications [30, 31], image encryption [32, 33], random number generation [34], watermarking [35], and chaos-based optimization [36].

Beyond structural multiplication of attractors, fractal sets and chaotic dynamics have been combined in several other directions. Mandelbrot and Julia sets have been used together with chaotic maps to generate keys and permutation–diffusion schemes for image encryption, for example, Julia-set keys combined with the Lorenz system [37], Mandelbrot-set keys combined with discrete chaotic maps [38, 39], and Julia sets combined with fractal dictionaries for joint compression and encryption [40]. Methods of chaos control and synchronization have been transferred to fractal sets, and controllers that deform or synchronize Julia sets of complex maps have been designed [41–43]. Finally, generalized Mandelbrot and Julia sets, in particular, sets of fractional order, have been studied as dynamical objects in their own right [43–46]: the fractional-order Mandelbrot and Julia sets defined through Caputo-like discrete fractional differences [44] show that the classical Mandelbrot set is recovered only in the limit of vanishing fractional order and is a particular fractional-order Julia set [46], and control and synchronization of fractional-order Julia sets have been achieved [43]. In the present work, only integer-order maps are used; the extension of the transformations to fractional-order Mandelbrot and Julia maps is a natural direction for future work. In these works, the fractal set serves mainly as a source of pseudo-random numbers or as an object of study and control. In the present work, by contrast, the Mandelbrot iteration is driven by the trajectory of a continuous-time memristive system and is used as a geometric transformation of its attractor, and the result is compared directly with the inverse-Julia (phase-space) transformations applied to the same attractor. While binary algorithms are naturally formulated for planar projections, many hyperchaotic systems evolve in higher-dimensional phase spaces. Extending fractal transformations to such systems requires careful selection of projection planes and appropriate algebraic structures for ternary mappings.

While inverse Julia set transformations effectively explore phase space dynamics with a fixed parameter, a complementary approach involves exploring the parameter space of the quadratic map $z \mapsto z^2 + c$ through forward iteration. This leads to transformations based on the Mandelbrot set, where chaotic sequences serve as the parameter c rather than the initial condition z_0. In this work, we introduce and investigate three novel Mandelbrot-based fractal transformation methods: the Mandelbrot orbit cloud (generating dense, nebula-like structures from accumulated orbits),

the Mandelbrot multiscroll expansion (producing geometrically regular patterns through iterative branching), and the fractal web (revealing the basin structure via multiple initial conditions). These methods generate distinct classes of attractors fundamentally different from those produced by inverse Julia maps, thereby expanding the toolkit for designing complex patterns from chaotic systems.

In this work, we study a four-dimensional memristive chaotic system composed of seven algebraic terms and lacking equilibrium points. This system was used in our recent work [47] as a source of chaotic modulation signals for the design of batik floral patterns, to which Julia- and Mandelbrot-based transformations were then applied; the dynamics of the system itself were not analyzed in detail there, and the transformations were applied to the modulated patterns rather than to the attractor.

System (2.3) differs from the related seven-term systems of [12–15] in the form of the memristive coupling: here, the memductance $\tanh x_4$ multiplies x_2 in the first equation and the flux is driven by x_2. The Julia fractal process itself is not new: It was introduced by Bouallegue et al. [26] and formalized by Dai et al. [29]. The contributions of the present paper therefore lie not in the system or in the Julia process as such, but in the combination of a detailed dynamical analysis of system (2.3) with a mathematical analysis of the transformations applied to its attractor.

In the present paper, we show that the system generates hidden chaotic attractors with one positive Lyapunov exponent; a detailed analysis of the Lyapunov spectrum shows that the memristor saturates along the trajectory, which gives rise to an additional neutral (zero) exponent associated with the flux variable. Multistability properties and phase-space structures are investigated, and circuit implementation in the Multisim environment confirms physical realizability. Building upon this dynamical foundation, we apply binary and ternary inverse Julia fractal transformations to phase-space projections of the proposed system. Systematic structural multiplication is demonstrated and quantitatively analyzed. We further investigate the geometric impact of different ternary multiplication rules and compare their structural outcomes. In addition, this paper provides a systematic study of Mandelbrot-based fractal transformations applied to a high-dimensional memristive system.

To position the present study with respect to the multi-scroll generation and fractal-transformation literature discussed above, Table 1 summarizes the main differences between our approach and the most closely related works. Compared with the binary inverse-Julia scheme of Bouallegue et al. [26–28] and the binary/ternary formalization of Dai et al. [29], the present work (i) applies the transformations to a 4D memristive chaotic system without equilibria, rather than to classical low-dimensional chaotic systems; (ii) introduces and compares two distinct ternary multiplication rules ($ij = -1$ and $ij = 0$), whereas [29] considers only $ij = 0$; and (iii) complements the inverse-Julia (phase-space) paradigm with three new Mandelbrot-based (parameter-space) transformation methods, in which the parameter of the Mandelbrot iteration is supplied by the trajectory of the continuous-time system (to the best of our knowledge, this use of the Mandelbrot iteration as a geometric transformation of a chaotic attractor has not been studied systematically before); and (iv) gives an analytical proof of the 2^N-fold structural multiplication (Proposition 1) and of the ternary inverse formulas (Proposition 2).

The remainder of the paper is organized as follows. Section 2 introduces the mathematical model of the proposed 4D memristive system. Section 3 provides a detailed dynamical analysis, covering the equilibrium structure, Lyapunov exponents, bifurcation behavior, multistability, phase portraits, Poincaré sections, spectral characteristics, and National Institute of Standards and Technology (NIST) randomness validation. Section 4 details the electronic circuit implementation of the proposed generator, simulated in the Multisim environment. Section 5 explores the application of binary and

ternary fractal algorithms to the generated attractors. Section 6 describes three distinct transformation algorithms based on the Mandelbrot set. Conclusions summarize the main findings.

Table 1. Comparison of the present study with representative multi-scroll generation methods and with closely related fractal-transformation works.

Work	Mechanism	Base system	Distinctive features
[16, 17]	Piecewise-linear nonlinearities	Autonomous chaotic systems	Modification of the vector field; non-smooth right-hand side
[18, 19]	Switching / discontinuous functions	Memristive chaotic systems	Modification of the vector field; non-smooth switching complicates analysis and implementation
Wan et al. [22]	Memristive autapse	Neuron model	Modification of the vector field; multiscroll hidden attractor; memristor-based control of the number of scrolls; image encryption
Wan et al. [23]	Memristor-based full-parameter control	Hopfield neural network	Modification of the vector field; robust construction of multiscroll structures via the memristor
Wan et al. [24]	State-based nonlinear mapping	Conservative oscillator	Modification of the vector field; cellular chaotic sea; hardware implementation
Bouallegue et al. [26–28]	Binary inverse Julia map (Julia process)	Classical chaotic systems	Post-processing of the trajectory; first "fractal process" for multi-scroll/multi-wing generation; planar projections; power-law doubling stated heuristically
Dai et al. [29]	Binary + ternary inverse Julia map ($ij = 0$)	Classical chaotic systems	Post-processing of the trajectory; systematic derivation; power law $M_2 = M_1 \cdot 2^N$; single ternary rule $ij = 0$; no memristive / no-equilibrium system
This work	Binary + ternary inverse Julia map ($ij = -1$ and $ij = 0$); three Mandelbrot-based methods	4D memristive system without equilibria (hidden attractor)	Post-processing of the trajectory without modification of the vector field; two ternary rules compared (anisotropic ribbons vs. isotropic tori); parameter-space (Mandelbrot) transformations: orbit cloud, multiscroll, fractal web; analytical proof of the 2^N-fold structural multiplication and of the ternary inverse formulas

2. Mathematical formulation of the 4D memristive dynamical system

We consider a four-dimensional memristive system (first used in [47]) obtained by extending the three-dimensional Munmuangsaen chaotic system from [48]. The original system contains five terms:

$$\begin{cases} \dfrac{dx_1}{dt} = a(-x_1 + x_2), \\ \dfrac{dx_2}{dt} = -x_1 x_3, \\ \dfrac{dx_3}{dt} = x_1 x_2 - b. \end{cases} \tag{2.1}$$

For parameters $a = 5, b = 90$ and initial conditions $x_1(0) = 5, x_2(0) = 10, x_3(0) = 5$, the system exhibits chaotic behavior with Lyapunov exponents $LE_1 = 1.4913, LE_2 = 0.0026, LE_3 = -6.4939$. As b increases from small positive values, the system undergoes a period-doubling cascade leading to chaos, consistent with the Feigenbaum scenario.

We incorporate a memristor element described by:

$$\begin{cases} i_m = W(\varphi)u_m, \\ \frac{d\varphi}{dt} = u_m, \\ W(\varphi) = \tanh\varphi, \end{cases} \tag{2.2}$$

where u_m and i_m are the voltage and current, φ is the flux, and $W(\varphi)$ is the memductance. This element exhibits pinched hysteresis loops under periodic excitation, with loop width depending on signal frequency and amplitude (see Figure 1). The resulting four-dimensional system is:

$$\begin{cases} \dfrac{dx_1}{dt} = a(-x_1 + x_2) - (\tanh x_4)x_2, \\ \dfrac{dx_2}{dt} = -x_1 x_3, \\ \dfrac{dx_3}{dt} = x_1 x_2 - b, \\ \dfrac{dx_4}{dt} = x_2, \end{cases} \tag{2.3}$$

where x_4 represents the memristor flux state. The system contains only seven terms, providing a minimal structure for generating complex dynamics in four dimensions.

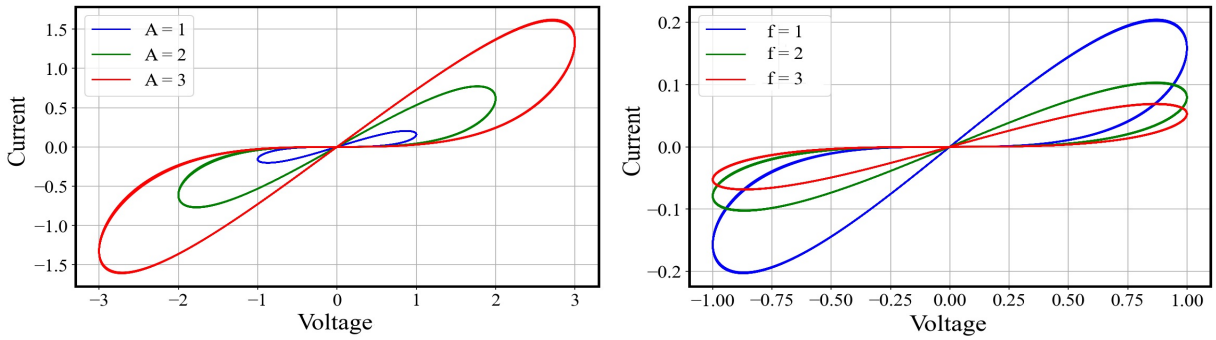


Figure 1. Pinched hysteresis loops of the memristor (2.2) driven by $u_m = A\sin(2\pi ft)$ (dimensionless time and frequency): left, fixed frequency $f = 1$ and amplitudes $A = 1, 2, 3$; right, fixed amplitude $A = 1$ and frequencies $f = 1, 2, 3$.

3. Dynamical analysis

In this section, we investigate the dynamical properties of the proposed 4D memristive system (2.3). We first examine its fundamental structural features, namely, the absence of any nontrivial sign symmetry of the vector field, the dissipativity established through the divergence, and the equilibrium structure, which reveals the hidden nature of the generated attractors. We then study the global dynamical evolution of the system as a function of the parameter b by means of bifurcation diagrams and the Lyapunov exponent spectrum, from which the Kaplan–Yorke dimension is subsequently evaluated (see Figures 2 and 3). The coexistence of multiple attractors (multistability) and the offset boosting control of the state variable x_3 are analyzed next. Finally, phase portraits, Poincaré cross-sections, power spectral density, NIST SP 800-22 randomness testing, and a Lyapunov-function-based boundedness analysis are employed to provide a complete characterization of the chaotic regime and to confirm the statistical quality of the generated sequences.

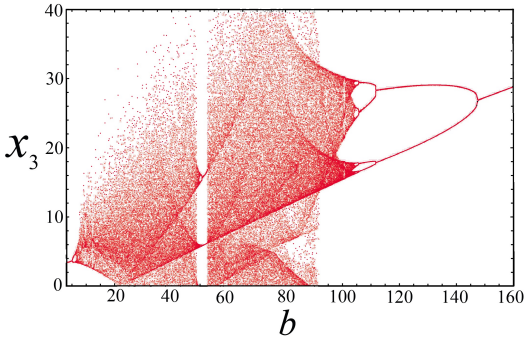


Figure 2. Bifurcation diagram of system (2.3) with respect to the parameter b for $a = 5$ and initial conditions (3.5), see page 9, shown for different ranges of b.

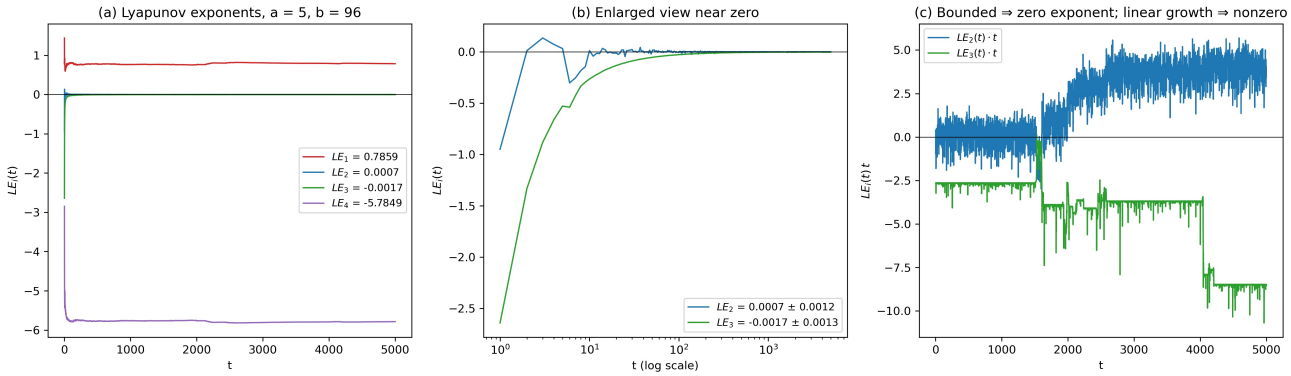


Figure 3. Convergence of the Lyapunov exponents of system (2.3) for $a = 5$, $b = 96$ and initial conditions (3.5) (transient $t \leq 200$ discarded, averaging time $T = 5000$): (a) all four exponents; (b) LE_2 and LE_3 on a logarithmic time axis; (c) the products $LE_2(t)\,t$ and $LE_3(t)\,t$, which remain bounded, as expected for vanishing exponents (a positive exponent λ would produce linear growth with slope λ).

3.1. Basic properties

Unlike its three-dimensional progenitor (2.1), which is invariant under $(x_1, x_2, x_3) \to (-x_1, -x_2, x_3)$, system (2.3) does not possess any nontrivial sign symmetry. Consider the candidate involution

$$S : (x_1, x_2, x_3, x_4) \to (-x_1, -x_2, x_3, -x_4). \tag{3.1}$$

Substituting S into the right-hand side of system (2.3) reproduces the second, third, and fourth equations, but fails for the first one because of the memristive coupling term. Indeed, under S, the term $-(\tanh x_4)x_2$ transforms as

$$-(\tanh(-x_4))(-x_2) = -(-\tanh x_4)(-x_2) = -(\tanh x_4)x_2, \tag{3.2}$$

i.e., it remains unchanged, whereas the odd part $a(-x_1 + x_2)$ of the first equation changes sign. Consequently, $\dot{\tilde{x}}_1 \neq -\dot{x}_1$, and the invariance condition $\mathbf{F}(S\,\mathbf{x}) = S\,\mathbf{F}(\mathbf{x})$ is violated. A direct check confirms that, among all sign-reversal maps $\mathrm{diag}(\pm1, \pm1, \pm1, \pm1)$, only the identity leaves

system (2.3) invariant. Thus the memristive term $(\tanh x_4)x_2$ breaks the symmetry inherited from the Munmuangsaen system, and the proposed system maps only onto itself. The absence of symmetry precludes symmetry-induced pairs of coexisting attractors; any multistability observed in Section 3.3 therefore arises solely from the nonlinear structure of the flow and the geometry of the basins of attraction.

The divergence of the vector field is:

$$\nabla \cdot \mathbf{F} = \frac{\partial \dot{x}_1}{\partial x_1} + \frac{\partial \dot{x}_2}{\partial x_2} + \frac{\partial \dot{x}_3}{\partial x_3} + \frac{\partial \dot{x}_4}{\partial x_4} = -a. \tag{3.3}$$

For $a > 0$, the system is dissipative with exponentially contracting phase space volume. Setting all derivatives to zero yields:

$$\begin{aligned} \dot{x}_4 = x_2 = 0, \\ \dot{x}_1 = -ax_1 = 0 \Rightarrow x_1 = 0, \\ \dot{x}_3 = -b = 0 \Rightarrow b = 0. \end{aligned} \tag{3.4}$$

For $b = 0$, equilibria form a continuum: $x_1 = x_2 = 0$, $x_3, x_4 \in \mathbb{R}$. Systems with a line of equilibria are commonly regarded as a class of systems that can exhibit hidden attractors in the sense of Leonov and Kuznetsov [49], provided that the basin of attraction does not intersect a neighborhood of any unstable equilibrium. For $b \neq 0$, no equilibrium exists, and the system generates hidden attractors in the strict sense.

It is worth clarifying the distinction between these two mechanisms, since both fall under the hidden-attractor classification of Leonov and Kuznetsov [49] but for different reasons. By definition, an attractor is self-excited if its basin of attraction intersects an arbitrarily small neighborhood of an unstable equilibrium, and hidden otherwise. In the first case realized by system (2.3), namely, $b = 0$, the equilibria degenerate into an invariant line $\{x_1 = x_2 = 0\}$; equilibria are present, but the attractor cannot be reached from their vicinity, so standard homoclinic/heteroclinic search procedures anchored to an unstable equilibrium are inapplicable. Such systems with a line or surface of equilibria have been studied, for instance, in [8, 9]. In the second case, $b \neq 0$, the right-hand side of the third equation, $\dot{x}_3 = x_1x_2 - b$, cannot vanish simultaneously with $\dot{x}_4 = x_2 = 0$, so the equilibrium set is empty. The attractor is then hidden in the strict, no-equilibrium sense, exemplified by the systems in [6, 11]; here, local linearization is not merely inconclusive but altogether undefined, since there is no point at which to linearize. The practical consequence, common to both regimes, is that the attractor cannot be localized or classified through any local (equilibrium-based) analysis.

Because neither regime allows a local analysis, we study the attractors of system (2.3) using global numerical tools. These include the analysis of coexisting basins (multistability), Poincaré sections, power spectra, and a Lyapunov function to assess boundedness. In the rest of this work, we use $b = 96$, which corresponds to the case without equilibria. Since the equilibrium set of system (2.3) is empty for every $b \neq 0$, no attractor of the system can have a basin intersecting a neighborhood of an equilibrium. Therefore, by the definition of Leonov and Kuznetsov [49], every attractor observed for $b \neq 0$, in particular, the chaotic attractor shown in Figure 4, is hidden; no numerical analysis of basins is required for this conclusion.

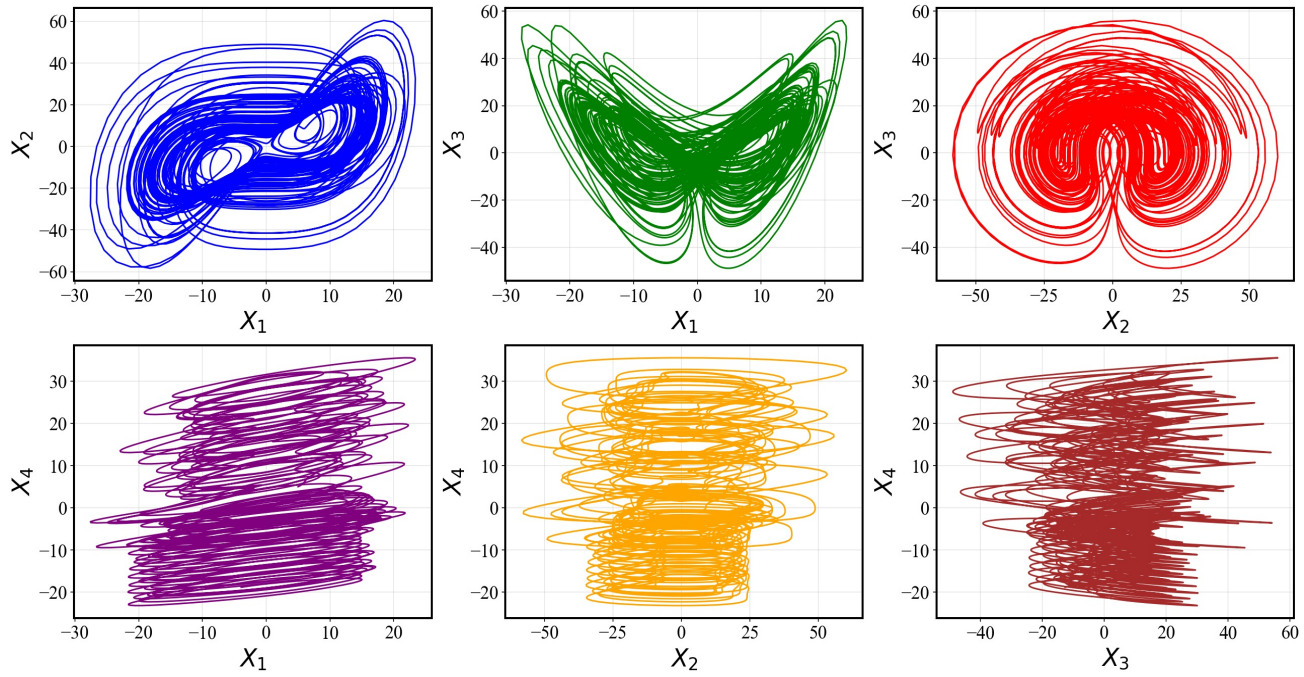


Figure 4. Phase portraits of the hidden chaotic attractor of system (2.3) for $a = 5$, $b = 96$ and initial conditions (3.5) in various planes. Since system (2.3) has no equilibria for $b \neq 0$ (Section 3.1), the attractor is hidden by definition.

3.2. Bifurcation analysis and Lyapunov exponents

We numerically integrated system (2.3) with the initial conditions:

$$x_1(0) = 5, \quad x_2(0) = 10, \quad x_3(0) = x_4(0) = 5, \tag{3.5}$$

fixing $a = 5$ and varying $b \in [3, 160]$. The bifurcation diagrams were constructed using the local extrema method implemented in Mathematica. Figure 2 presents the bifurcation diagram of the system as a function of parameter b. A complex dynamical evolution is observed, characterized by alternating regions of chaos and periodic windows. As b increases, the system exhibits a period-doubling cascade leading to developed chaos, which subsequently transitions into a stable limit cycle for $b > 150$.

Lyapunov exponents were computed using the algorithms of [50, 51]. We validated our implementation by computing exponents for system (2.1):

$$LE_1 = 1.43053, \quad LE_2 = 0.003349, \quad LE_3 = -6.43537, \tag{3.6}$$

which agree well with [48]. For system (2.3), the variational equations were integrated with an adaptive eighth-order Runge–Kutta (Dormand–Prince) scheme with relative and absolute tolerances 10^{-10}; the tangent vectors were re-orthonormalized by the orthogonal–triangular (QR) decomposition at unit time intervals, a transient of length $t = 200$ was discarded, and the exponents were averaged over $T = 5000$. The statistical uncertainty σ_i of each exponent was estimated as the standard error of the finite-time exponents computed on 20 consecutive blocks of length $T/20$. An exponent is classified as zero if $|LE_i| < 3\sigma_i$, and as positive or negative otherwise; for all exponents classified as zero, $3\sigma_i \leq 0.008$.

As an independent accuracy check, we use the exact identity $\sum_{i=1}^{4} LE_i = \langle \nabla \cdot \mathbf{F} \rangle = -a = -5$, which is satisfied by all entries of Table 2 to within 10^{-4}. Table 2 classifies the dynamical behavior for various values of b based on this criterion. For $b = 110$ and $b = 140$, the finite-time exponents did not converge within $T = 5000$ ($\sigma_1 \approx 0.1$), which indicates long chaotic transients or switching between coexisting attractors; these values are therefore not included in the table.

In every regime, the spectrum contains one more vanishing exponent than the single zero exponent associated with the direction of the flow. Its origin is the memristor. The flux variable obeys the pure integrator $\dot{x}_4 = x_2$ and is undamped; along the trajectory, x_4 drifts slowly and, after a short transient, stays far from the origin. For $b = 96$, we found $|\tanh x_4| > 0.99$ during about 99% of the integration time, and for the other values of b in Table 2, this fraction is practically 100%. In this saturated regime, the memductance is effectively constant, $\tanh x_4 \approx \varsigma = \pm 1$, the variables (x_1, x_2, x_3) evolve according to

$$\dot{x}_1 = -a\, x_1 + (a - \varsigma)\, x_2, \qquad \dot{x}_2 = -x_1 x_3, \qquad \dot{x}_3 = x_1 x_2 - b, \tag{3.7}$$

and perturbations of x_4 are neither amplified nor damped, since $\partial \dot{x}_1 / \partial x_4 = -x_2 \operatorname{sech}^2 x_4 \approx 0$. This neutral direction produces the additional zero exponent. Consequently, the signatures $(0, 0, -, -)$ and $(+, 0, 0, -)$ in Table 2 correspond to periodic and chaotic oscillations of (x_1, x_2, x_3), respectively, accompanied by the neutral drift of the flux x_4, and a second positive exponent (hyperchaos) cannot occur while the memristor is saturated. The memristor acts mainly during transients and whenever x_4 changes sign, switching the effective coefficient $a - \varsigma$ in (3.7). The convergence of LE_2 and LE_3 to zero is illustrated in Figure 3(b),(c).

Table 2. Lyapunov exponents of system (2.3) ($a = 5$, initial conditions (3.5)) for different values of b (mean $\pm\sigma$; averaging time $T = 5000$). An exponent is classified as zero if $|LE_i| < 3\sigma_i$.

b	LE_1	LE_2	LE_3	LE_4	Signs	Behavior
3	0.0009 ± 0.0005	-0.0003 ± 0.0003	-0.0041 ± 0.0012	-4.9965 ± 0.0012	$(0, 0, -, -)$	Periodic
10	0.0381 ± 0.0106	0.0005 ± 0.0008	-0.0015 ± 0.0025	-5.0371 ± 0.0093	$(+, 0, 0, -)$	Weakly chaotic
15	0.7789 ± 0.0062	0.0004 ± 0.0006	-0.0008 ± 0.0006	-5.7784 ± 0.0061	$(+, 0, 0, -)$	Chaotic
60	1.3568 ± 0.0137	0.0002 ± 0.0009	-0.0003 ± 0.0003	-6.3567 ± 0.0138	$(+, 0, 0, -)$	Chaotic
78	0.0002 ± 0.0010	-0.0004 ± 0.0004	-1.2925 ± 0.0013	-3.7072 ± 0.0018	$(0, 0, -, -)$	Periodic
93	0.8438 ± 0.0071	0.0005 ± 0.0008	-0.0010 ± 0.0009	-5.8433 ± 0.0067	$(+, 0, 0, -)$	Chaotic
96	0.7859 ± 0.0229	0.0007 ± 0.0012	-0.0017 ± 0.0013	-5.7849 ± 0.0228	$(+, 0, 0, -)$	Chaotic
97	0.9301 ± 0.0730	0.0003 ± 0.0009	-0.0016 ± 0.0020	-5.9288 ± 0.0732	$(+, 0, 0, -)$	Chaotic
160	0.0003 ± 0.0004	-0.0009 ± 0.0003	-0.4066 ± 0.0002	-4.5927 ± 0.0002	$(0, 0, -, -)$	Periodic

For $b = 96$, the system is chaotic with one positive Lyapunov exponent (Figure 3); the sum of the exponents equals -5.0000, in agreement with $\nabla \cdot \mathbf{F} = -a$. The Kaplan–Yorke dimension is:

$$D_{KY} = 3 + \frac{LE_1 + LE_2 + LE_3}{|LE_4|} = 3 + \frac{0.7849}{5.7849} \approx 3.136. \tag{3.8}$$

Because one of the vanishing exponents corresponds to the neutral flux direction rather than to the geometry of the attractor, this value has to be interpreted with care: for the chaotic set of the (x_1, x_2, x_3) dynamics, excluding the neutral direction, one obtains $D_{KY} \approx 2.14$, comparable to $D_{KY} = 2.2301$ of

system (2.1). For $a = 5$, $b = 96$ with initial conditions (3.5), Figure 4 shows phase portraits in multiple projection planes, revealing complex geometric structures of the chaotic attractor.

3.3. Multistability analysis and offset boosting control

Multistability, defined as the coexistence of multiple attractors within a single dynamical system, represents a fundamental phenomenon wherein distinct attracting states emerge depending on the choice of initial conditions (see, for example, [10]). This characteristic enables dynamical systems to exhibit multiple stable behaviors under identical parameter conditions. Since system (2.3) possesses no nontrivial symmetry (Section 3.1), the coexisting attractors it exhibits are not related by any sign-reversal map; the multistability observed here originates from the nonlinear structure of the flow and the geometry of the basins of attraction. To investigate this multistable behavior, we integrated the system from two initial conditions with reversed signs in the odd variables,

$$\mathbf{B}_0 = (5,\ 10,\ 5,\ 5), \qquad \mathbf{R}_0 = (-5,\ -10,\ 5,\ -5),$$

and found that they converge to distinct coexisting attractors.

Figure 5 illustrates the distinct attractor trajectories obtained from initial conditions $\mathbf{B}_0$ and $\mathbf{R}_0$, presented in the (x_1, x_3) and (x_2, x_3) projection planes, with blue trajectories corresponding to $\mathbf{B}_0$ and red trajectories corresponding to $\mathbf{R}_0$. Three distinct parameter regimes demonstrate the versatility of multistable behavior in system (2.3).

For $b = 3$, the system exhibits two coexisting periodic attractors (Figure 5(a)). The blue attractor originating from $\mathbf{B}_0$ and the red attractor from $\mathbf{R}_0$ occupy geometrically distinct and spatially separated regions of the phase space, with no overlap between their trajectories. The corresponding time series of $x_1(t)$ for each initial condition confirm regular periodic oscillations with different amplitudes, consistent with the Lyapunov exponent classification in Table 2.

At the parameter value $b = 96$, the system demonstrates chaotic behavior with one positive Lyapunov exponent (Figure 5(b)). The phase portraits reveal that the two attractors, while sharing a broadly similar butterfly-like topology, exhibit distinctly different spatial extents: The attractor from $\mathbf{B}_0$ reaches significantly larger amplitudes in the x_3 direction (up to ± 100) compared with that from $\mathbf{R}_0$ (up to ± 35), confirming the coexistence of two qualitatively similar yet geometrically distinguishable chaotic attractors.

For $b = 110$, the Lyapunov exponents converge very slowly (Section 3.1), which indicates long chaotic transients; nevertheless, the phase portraits in Figure 5(c) again display two coexisting attractors with different structural characteristics: The attractor from $\mathbf{B}_0$ exhibits a more complex multi-lobed geometry with larger spatial extent, while the attractor from $\mathbf{R}_0$ is more compact. This distinction is corroborated by the time series, which show aperiodic oscillations with markedly different envelope structures for the two initial conditions.

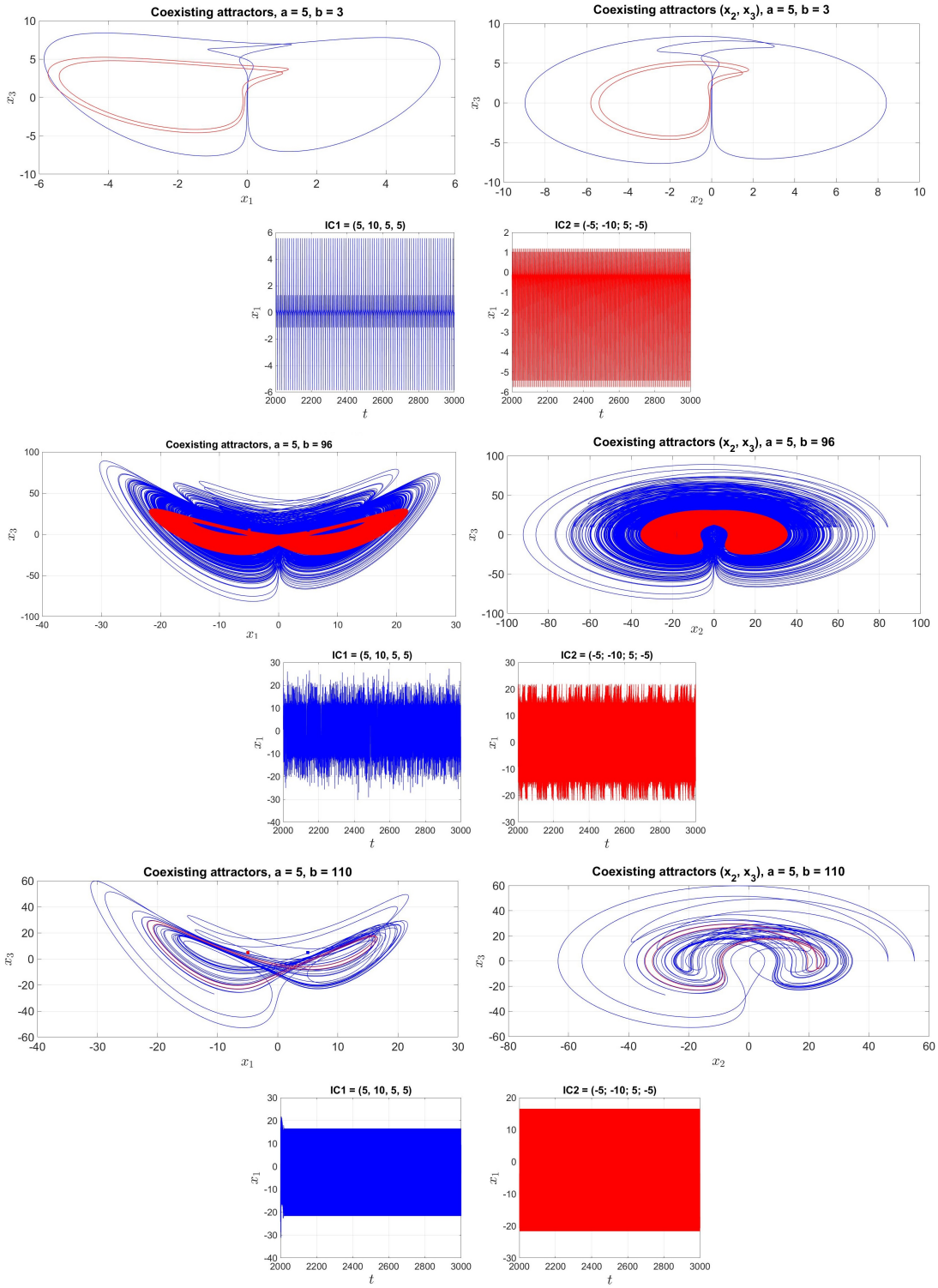


Figure 5. Coexisting attractors of system (2.3) for $a = 5$ and initial conditions $\mathbf{B}_0 = (5, 10, 5, 5)$ (blue) and $\mathbf{R}_0 = (-5, -10, 5, -5)$ (red): phase portraits in the (x_1, x_3) and (x_2, x_3) planes and time series of $x_1(t)$. (a) $b = 3$, two coexisting periodic attractors; (b) $b = 96$, two coexisting chaotic attractors of different spatial extent; (c) $b = 110$, two coexisting aperiodic attractors of different spatial extent.

The coexistence of multiple attractors across a wide range of the parameter b may indicate complex basin boundaries in the initial condition space. Any use of the system in chaos-based communication would require synchronization between transmitter and receiver; recent advances in fast fixed-time synchronization of multi-layer networks [52] and event-triggered synchronization of multi-agent networked systems with time-varying delays [53] provide effective control frameworks that could be adapted to synchronize the proposed chaotic system, which we identify as a direction for future work.

The offset boosting control method is a robust technique for chaotic and hyperchaotic systems, facilitating the flexible shifting of attractors through the introduction of an offset. This approach is highly advantageous for engineering applications (see, for example, [54]), as it enables the manipulation of chaotic signals across the phase space by adding constant offsets to specific variables. In system (2.3), the state variable x_3 appears solely in the second equation, making it a natural candidate for control. Substituting x_3 with $x_3 + k$ (where k is a constant) allows for direct control over the signal's position.

Figure 6 illustrates the impact of the offset parameter k: A positive value ($k = 55$) shifts the attractor (green) in the negative direction, while a negative value ($k = -55$) moves the attractor (red) in the positive direction. The blue attractor represents the baseline state where $k = 0$ (no shift). According to the third equation of system (2.3), the attractor's range along the x_3 coordinate remains invariant for any constant k. Conversely, the x_2 coordinate exhibits a change in scale; this is particularly evident in the red attractor, where a negative k leads to an expansion of x_2 as dictated by the second equation of system (2.3). As shown in the left panel of Figure 6, adjusting the offset parameter k effectively transitions the x_3 signal from a bipolar to a unipolar configuration. Simultaneously, as depicted in the right panel, modifying k facilitates a precise spatial shift of the attractor along the x_3-axis.

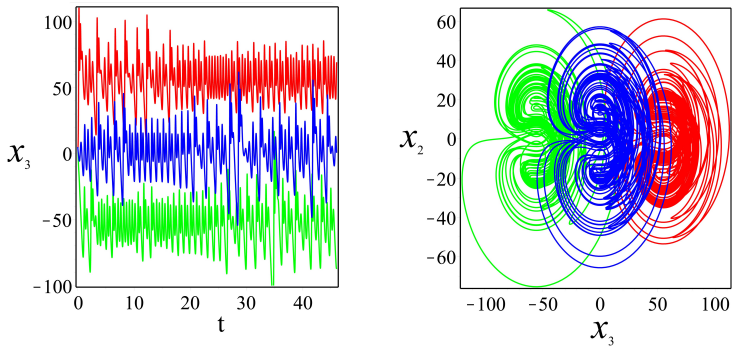


Figure 6. Time-domain signal x_3 and phase portraits in the x_3x_2 plane of system (2.3) with $x_3 \to x_3 + k$ ($a = 5$, $b = 96$) for varying offset boosting levels: $k = 0$ (blue), $k = 55$ (green), and $k = -55$ (red).

Figure 7 illustrates the bifurcation diagram highlighting the phenomena of multistability and offset boosting control. The blue trajectories correspond to the baseline initial conditions $(5, 10, 5, 5)$ without offset. The green and red diagrams represent the system behavior for initial conditions $(-5, -10, 5, -5)$ with offset boosting parameters $k = 20$ and $k = -20$, respectively. The overlapping plots demonstrate that varying the initial conditions and the control parameter k allows coexisting attractors to be precisely shifted along the x_3-axis. The identical bifurcation structures across different offsets confirm the robustness of the offset boosting method in manipulating signal positioning within multistable

chaotic systems.

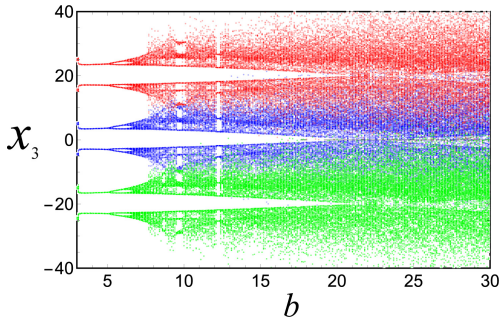


Figure 7. Bifurcation diagrams of system (2.3) with $x_3 \to x_3 + k$ ($a = 5$) versus b, showing multistability under offset boosting for different initial conditions and control parameters: $k = 0$ (blue), $k = 20$ (green), and $k = -20$ (red).

3.4. Power spectra analysis

Figure 8 shows the power spectra of systems (2.1) and (2.3). Both spectra exhibit a broadband, noise-like structure characteristic of deterministic chaos, with power decaying continuously over the whole range of (dimensionless) frequencies shown and no dominant periodic components, confirming the presence of strange attractors in both systems. A pronounced sharp peak at $f \approx 200$ and secondary spectral elevations in the band $f \approx 500$–600 are visible in both curves, indicating that the fundamental low-frequency dynamical features of the original system are preserved in the memristive extension. A key observation, however, is that the spectrum of the memristive system does not merely replicate that of its three-dimensional progenitor. As seen in Figure 8, the blue curve largely overlaps with the red one, meaning that the new system captures the entire spectral content of the original Munmuangsaen system. Beyond this shared region, distinct segments of the blue spectrum are visible that have no counterpart in the red curve. These exclusive spectral components, appearing at various frequency intervals across the full range, are intrinsic to the four-dimensional memristive system and reflect dynamical modes that emerge solely due to the memristive coupling term $(\tanh x_4)\, x_2$.

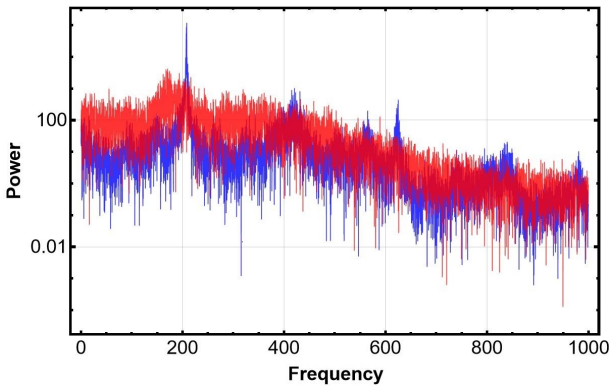


Figure 8. Power spectra of system (2.3) ($a = 5$, $b = 96$, initial conditions (3.5)) (blue), and system (2.1) (red).

This spectral enrichment is consistent with the increase in attractor dimensionality: The Kaplan–Yorke dimension of the original system is $D_{KY} = 2.2301$, while for the memristive system, it reaches $D_{KY} \approx 3.159$. The higher-dimensional attractor occupies a substantially larger region of phase space, giving rise to additional degrees of freedom in the dynamics that manifest directly as new spectral components absent in the original system.

3.5. Poincaré section analysis

Poincaré maps provide dimension-reduction diagnostic tools for analyzing attractor topology by recording state vectors at successive intersections with a prescribed hyperplane. We construct three cross-sections to expose the system's internal structure. The first section is defined by the hyperplane $x_3 = 2.5$ with trajectories projected onto the (x_1, x_4) plane. This choice exploits the role of x_3 in coupling terms: It appears in the quadratic nonlinearity x_1x_2 governing $\dot{x}_3$ and directly influences $\dot{x}_2 = -x_1x_3$, making this plane sensitive to nonlinear dynamics. The second section uses $x_2 = 5$ projected onto (x_1, x_4). Since x_2 couples to all four equations appearing explicitly as $\dot{x}_4 = x_2$ and in the memristive feedback term $-(\tanh x_4)x_2$, this hyperplane captures cross-variable interactions throughout the phase space. The third section at $x_1 = 0$ is analyzed in the (x_2, x_4) projection. Variable x_1 drives the nonlinear product terms in both $\dot{x}_2$ and $\dot{x}_3$, so the hyperplane $x_1 = 0$ separates regions of opposite twisting in the flow, and is frequently traversed by the trajectories, rendering it geometrically informative.

Figure 9 displays the resulting Poincaré maps, which exhibit irregular fractal point distributions without discernible periodic structure. These scattered clouds confirm the absence of low-period orbits and are consistent with the chaotic classification established through Lyapunov analysis. Note that the spread along x_4 also reflects the slow drift of the flux variable discussed in Section 3.1.

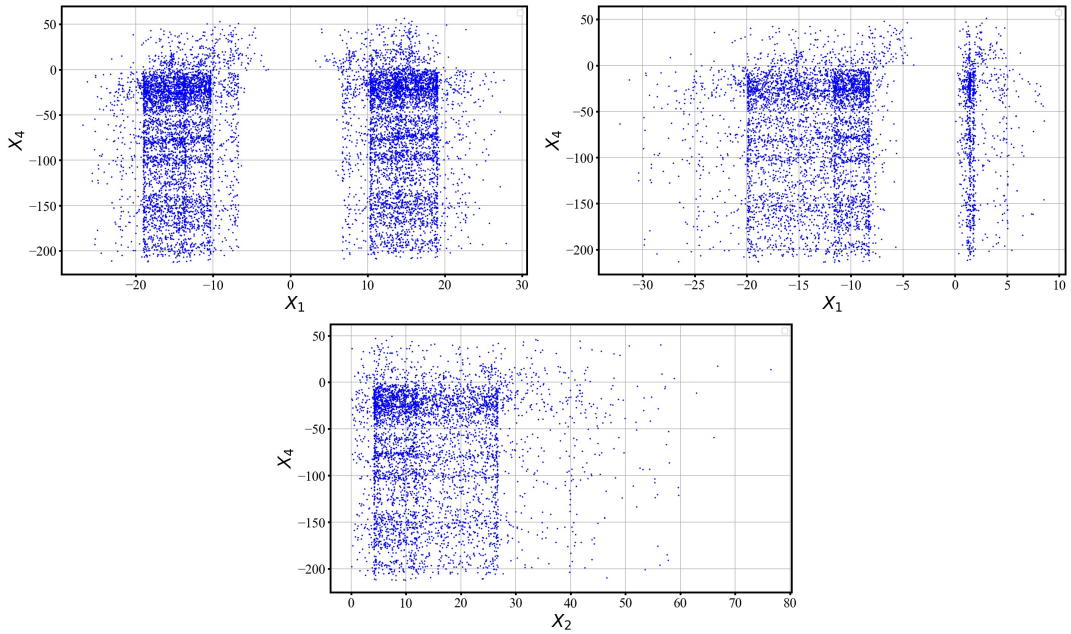


Figure 9. Poincaré sections of system (2.3) for $a = 5$, $b = 96$, and initial conditions (3.5): hyperplane $x_3 = 2.5$ projected onto (x_1, x_4); hyperplane $x_2 = 5$ projected onto (x_1, x_4); hyperplane $x_1 = 0$ projected onto (x_2, x_4).

3.6. Lyapunov stability analysis

To assess trajectory boundedness, we consider the radial quadratic function

$$V(\mathbf{x}) = \frac{1}{2}\left(x_1^2 + x_2^2 + x_3^2 + x_4^2\right), \tag{3.9}$$

whose derivative along the trajectories of system (2.3) is

$$\dot{V} = x_1\dot{x}_1 + x_2\dot{x}_2 + x_3\dot{x}_3 + x_4\dot{x}_4 = -a\,x_1^2 + a\,x_1x_2 - x_1x_2\tanh x_4 - b\,x_3 + x_2x_4, \tag{3.10}$$

where the cubic terms $-x_1x_2x_3$ and $+x_1x_2x_3$ arising from $x_2\dot{x}_2$ and $x_3\dot{x}_3$ cancel identically. We now bound each indefinite term in (3.10) using Young's inequality $pq \le \frac{\varepsilon}{2}p^2 + \frac{1}{2\varepsilon}q^2$ ($\varepsilon > 0$), the Cauchy–Schwarz inequality, and $|\tanh x_4| \le 1$:

$$a\,x_1x_2 \le \frac{a\varepsilon_1}{2}\,x_1^2 + \frac{a}{2\varepsilon_1}\,x_2^2, \tag{3.11}$$

$$-x_1x_2\tanh x_4 \le |x_1x_2| \le \frac{1}{2}\,x_1^2 + \frac{1}{2}\,x_2^2, \tag{3.12}$$

$$x_2x_4 \le \frac{1}{2}\,x_2^2 + \frac{1}{2}\,x_4^2, \tag{3.13}$$

$$-b\,x_3 \le \frac{1}{2}\,b^2 + \frac{1}{2}\,x_3^2. \tag{3.14}$$

Substituting (3.11)–(3.14) into (3.10) gives

$$\dot{V} \le -\Big(a - \tfrac{a\varepsilon_1}{2} - \tfrac{1}{2}\Big)x_1^2 + \Big(\tfrac{a}{2\varepsilon_1} + 1\Big)x_2^2 + \tfrac{1}{2}\,x_3^2 + \tfrac{1}{2}\,x_4^2 + \tfrac{1}{2}b^2. \tag{3.15}$$

Proposition. *No estimate of the form $\dot{V} \le -\kappa V + C$ with $\kappa > 0$ can be obtained from (3.9) for system (2.3); consequently, a single global compact bounding region for (x_1, x_2, x_3, x_4) cannot be derived by this quadratic Lyapunov method.*

Proof. In the quadratic form on the right-hand side of (3.15), the coefficients of x_2^2, x_3^2, and x_4^2 are strictly positive for every choice of $\varepsilon_1 > 0$; only the x_1^2 coefficient can be made negative. This is not a consequence of the limiting inequalities, but a structural property of the system: The divergence $\nabla \cdot \mathbf{F} = -a$ (Eq (3.3)) shows that contraction acts on the x_1 direction alone, since $\partial\dot{x}_2/\partial x_2 = \partial\dot{x}_3/\partial x_3 = \partial\dot{x}_4/\partial x_4 = 0$. In particular, the flux variable x_4 obeys the pure integrator $\dot{x}_4 = x_2$ and is undamped, entering $\dot{V}$ only through the sign-indefinite term x_2x_4, while the constant forcing $-b$ in $\dot{x}_3$ produces the sign-indefinite linear term $-b\,x_3$. Hence the right-hand side of (3.15) cannot be majorized by $-\kappa V + C$ with $\kappa > 0$, and no sublevel set $\{V \le \ell\}$ is rendered forward invariant. Equivalently, setting $x_1 = 0$ in (3.10) yields $\dot{V} = -b\,x_3 + x_2x_4$, which tends to $+\infty$ along $x_2 = x_4 = 0$, $x_3 \to -\infty$, and along $x_3 = 0$, $x_2 = x_4 \to \infty$, so $\dot{V}$ is positive and unbounded on directions escaping to infinity. □

The proposition shows that, for this equilibrium-free memristive system, a closed-form compact bound obtained from a quadratic Lyapunov function via the Young and Cauchy–Schwarz inequalities is not available: The behavior of the flux $x_4(t) = x_4(0) + \int_0^t x_2\,dt$ is determined by the long-time statistics of x_2 and cannot be certified by V. Boundedness is therefore examined numerically. Over the long interval $t \in [0, 10^4]$, the variables (x_1, x_2, x_3) remain bounded,

$$|x_1| \le 34, \qquad |x_2| \le 86, \qquad |x_3| \le 83, \tag{3.16}$$

whereas the flux x_4 performs a slow irregular drift of growing amplitude (over the same interval x_4 ranged from -134 to 549). This drift does not affect the dynamics of (x_1, x_2, x_3) once the memristor is saturated, and it is the origin of the neutral Lyapunov direction discussed in Section 3.1. Figure 10 shows $V(t)$ on the interval $t \in [0, 600]$; on longer time scales, V grows slowly because of the drift of x_4. Thus the chaotic attractor is bounded in the (x_1, x_2, x_3) subspace, in agreement with the dissipativity $\nabla \cdot \mathbf{F} = -a < 0$ and with the bounded support of the Poincaré sections in Section 3.5, while the flux x_4 is not confined, in agreement with the proposition above.

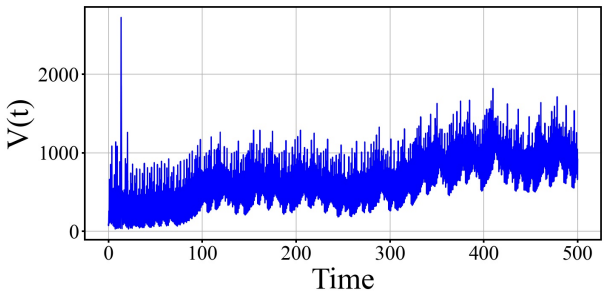


Figure 10. Time evolution of the quadratic function $V(t)$ along the trajectory of system (2.3) for $a = 5$, $b = 96$, and initial conditions (3.5) on the interval $t \in [0, 600]$.

3.7. Sensitivity to initial conditions

Chaotic dynamics exhibit exponential amplification of initial perturbations along the unstable direction. To quantify this sensitivity, we compare two trajectories with initial conditions differing by $\Delta x_1(0) = 0.0001$: The reference trajectory starts at $x_1(0) = 5$ (blue curve in Figure 11), while the perturbed trajectory begins at $x_1(0) = 5.0001$ (yellow curve). All other initial conditions and parameters remain identical.

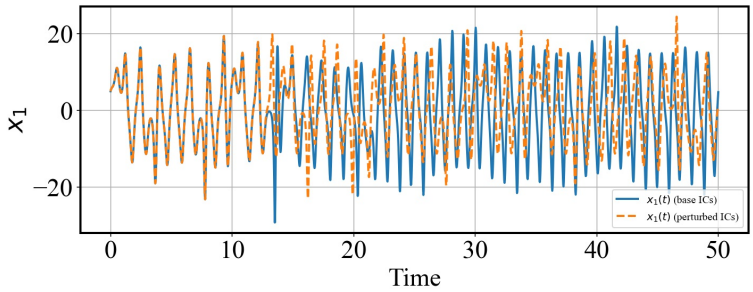


Figure 11. Temporal evolution of $x_1(t)$ of system (2.3) ($a = 5$, $b = 96$) for two initial conditions differing by $\Delta x_1(0) = 10^{-4}$, demonstrating the exponential divergence characteristic of chaotic dynamics.

Figure 11 demonstrates that the trajectories initially evolve in close proximity but diverge noticeably after $t \approx 12$ (dimensionless time). This rapid decorrelation arises from the positive Lyapunov exponent $LE_1 \approx 0.79$. The resulting exponential divergence rate $\|\delta\mathbf{x}(t)\| \sim e^{LE_1 t}$ implies that infinitesimal measurement uncertainties or numerical round-off errors grow rapidly, rendering long-term trajectory prediction infeasible.

3.8. Testing the randomness of chaotic sequences

To evaluate the statistical properties of the binary sequences generated by system (2.3) with initial conditions (3.5), we applied the NIST SP 800-22 test suite using a Python implementation. The bit sequence was extracted from the x_3 component of the trajectory and processed via Von Neumann debiasing to eliminate any residual bias inherent to the chaotic signal, yielding a balanced sequence of 149,705 bits with a mean value of 0.5006. Table 3 presents the results of all 15 statistical tests. In accordance with NIST standards [55], a sequence is considered to pass a given test if the corresponding p-value exceeds the significance threshold $\alpha = 0.01$. The proposed system successfully passed all 15 tests with a pass rate of 100%, with p-values ranging from 0.025 to 1.000, all above the threshold. These results confirm that the generated sequences possess good pseudo-random properties. We emphasize that this test characterizes only the statistical properties of the generated sequences; the design and security analysis of a cryptographic scheme is beyond the scope of this work.

Table 3. Results of the NIST SP 800-22 randomness tests for a 149,705-bit chaotic sequence extracted from $x_3(t)$ of system (2.3) ($a = 5$, $b = 96$).

No.	Test name	p-value	Result
1	Frequency (Monobit) Test	0.32102	PASS
2	Block Frequency Test	0.24867	PASS
3	Runs Test	0.77285	PASS
4	Longest Run of Ones in a Block Test	0.46533	PASS
5	Binary Matrix Rank Test	0.31533	PASS
6	Discrete Fourier Transform (Spectral) Test	0.53195	PASS
7	Non-overlapping Template Matching Test	0.99738	PASS
8	Overlapping Template Matching Test	0.55351	PASS
9	Universal Statistical Test (Maurer's)	0.99221	PASS
10	Linear Complexity Test	0.51214	PASS
11	Serial Test	0.79029	PASS
12	Approximate Entropy Test	0.82067	PASS
13	Cumulative Sums Test (Forward)	0.99986	PASS
14	Cumulative Sums Test (Backward)	1.00000	PASS
15	Random Excursions Variant Test	0.02520	PASS

4. Electronic circuit implementation

In this section, we develop an electronic circuit for implementing a four-dimensional (4D) memristive chaotic system (2.3). The design utilizes operational amplifiers and a well-established electronic circuit for implementing the hyperbolic tangent function [56]. However, as shown in Figure 4, the dynamic variables x_i ($i = 1, 2, 3, 4$) exceed the range supported by the op-amp power supply. To address this limitation, the variables x_i in the dynamic system (2.3) are scaled as follows:

$$x_1 = 10X_1, \quad x_2 = 20X_2, \quad x_3 = 20X_3, \quad x_4 = 20X_4. \tag{4.1}$$

Accordingly, the initial conditions (3.5) are transformed as follows:

$$X_1(0) = 0.5, \quad X_2(0) = 0.5, \quad X_3(0) = 0.25, \quad X_4(0) = 0.25. \tag{4.2}$$

In the rescaled system (2.3), we represent the state variables as electrical signals corresponding to the instantaneous voltage values across the capacitors C_i, denoted as $u_i(\tau)$. Then, in accordance with Kirchhoff's laws for electrical circuits, we obtain

$$\begin{cases} C_1 \dfrac{du_1}{d\tau} = -\dfrac{u_1}{R_1} + \dfrac{u_2}{R_2} - \dfrac{\tanh(u_4)u_2}{R_3 \cdot K}, \\ C_2 \dfrac{du_2}{d\tau} = -\dfrac{u_1 u_3}{R_4 \cdot K}, \\ C_3 \dfrac{du_3}{d\tau} = \dfrac{u_1 u_2}{R_5 \cdot K} - \dfrac{\widetilde{V}_b}{R_6}, \\ C_4 \dfrac{du_4}{d\tau} = \dfrac{u_2}{R_7}, \end{cases} \tag{4.3}$$

where $\widetilde{V}_b$ is a stable DC voltage source, R_k are resistors ($k = 1, 2, 3, 4, 5, 6, 7$), $u_i(\tau)$ are the capacitor voltages, C_i are capacitors, and K is a scaling coefficient for the multiplier. We choose the normalized resistor as $R_0 = 100$ kΩ and the capacitor as $C_0 = 1$ nF, giving a time constant of $t_0 = R_0 C_0 = 10^{-4}$ s. To obtain a dimensionless form of system (4.3), we perform the following rescaling of state variables: $u_i = U_0 \widetilde{X}_i$ for $i = 1, 2, 3, 4$, along with $K = U_0 K'$ and $\tau = t_0 t$, where U_0 represents a voltage normalization constant. Substituting the values R_0, $C_1 = C_2 = C_3 = C_4 = C_0$, and $K' = 10$ into (4.3) yields

$$\begin{cases} \dfrac{d\widetilde{X}_1}{dt} = -\dfrac{100\text{k}}{R_1}\widetilde{X}_1 + \left(\dfrac{100\text{k}}{R_2} - \dfrac{100\text{k}}{R_3 \cdot 10}\tanh(\widetilde{X}_4)\right)\widetilde{X}_2, \\ \dfrac{d\widetilde{X}_2}{dt} = -\dfrac{100\text{k}}{R_4 \cdot 10}\widetilde{X}_1\widetilde{X}_3, \\ \dfrac{d\widetilde{X}_3}{dt} = \dfrac{100\text{k}}{R_5 \cdot 10}\widetilde{X}_1\widetilde{X}_2 - \dfrac{100\text{k}}{R_6}V_b, \\ \dfrac{d\widetilde{X}_4}{dt} = \dfrac{100\text{k}}{R_7}\widetilde{X}_2, \end{cases} \tag{4.4}$$

where

$$R_1 = 20\,\text{k}\Omega,\ R_2 = 10\,\text{k}\Omega,\ R_3 = 5\,\text{k}\Omega,\ R_4 = R_5 = 1\,\text{k}\Omega,\ R_6 = 20.83\,\text{k}\Omega,\ R_7 = 100\,\text{k}\Omega,\ V_b = 1\,V.$$

Figure 12 illustrates analog circuit modules for the equations of system (4.4). These circuits incorporate standard components, including resistors (R), capacitors (C), multipliers M_1–M_3 (AD633), operational amplifiers $A1$–$A15$ (TL084ACN), and a supply voltage of ±15V. To implement the hyperbolic tangent function tanh, a standard electronic circuit [56] is used, as shown in Figure 13.

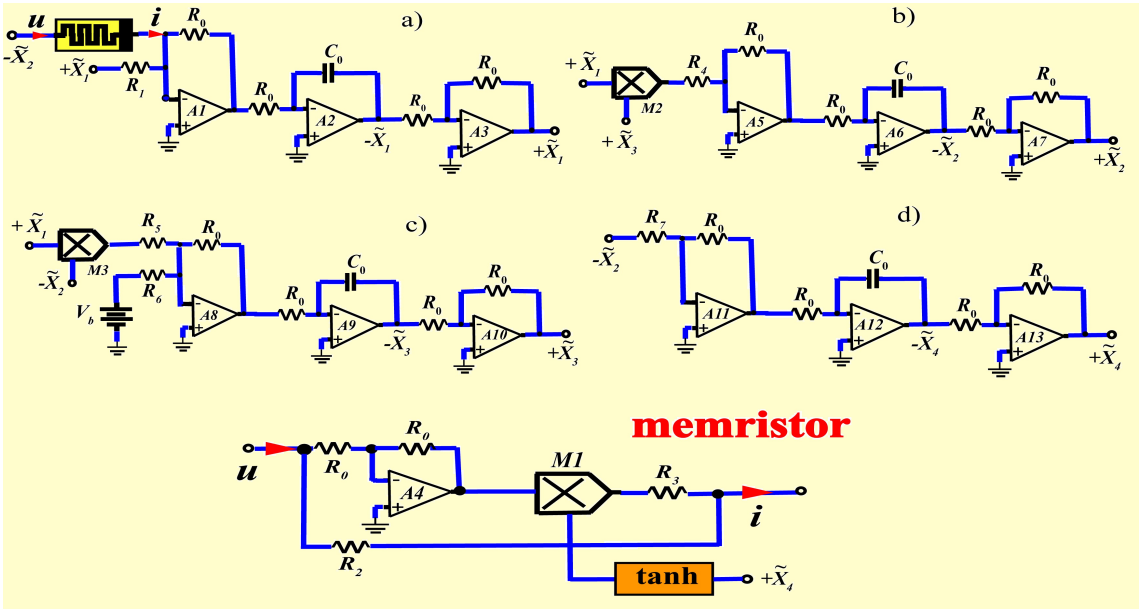


Figure 12. Circuit modules implemented based on a system of equations (4.4): a) $\widetilde{X}_1$, b) $\widetilde{X}_2$, c) $\widetilde{X}_3$, d) $\widetilde{X}_4$, and the memristor circuit module.

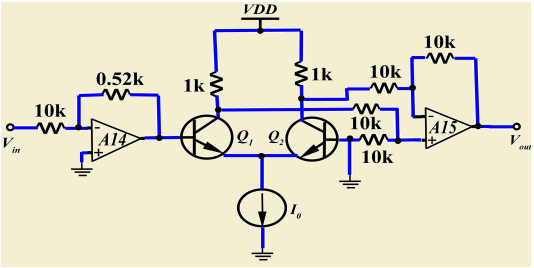


Figure 13. Circuit scheme for realization of hyperbolic tangent function.

The phase portraits in Figure 14, obtained from the Multisim circuit simulation, are in close agreement with those in Figure 4, obtained from the numerical integration of system (2.3). This consistency between the circuit simulation results and the numerical simulation results confirms the physical realizability of the proposed chaotic system.

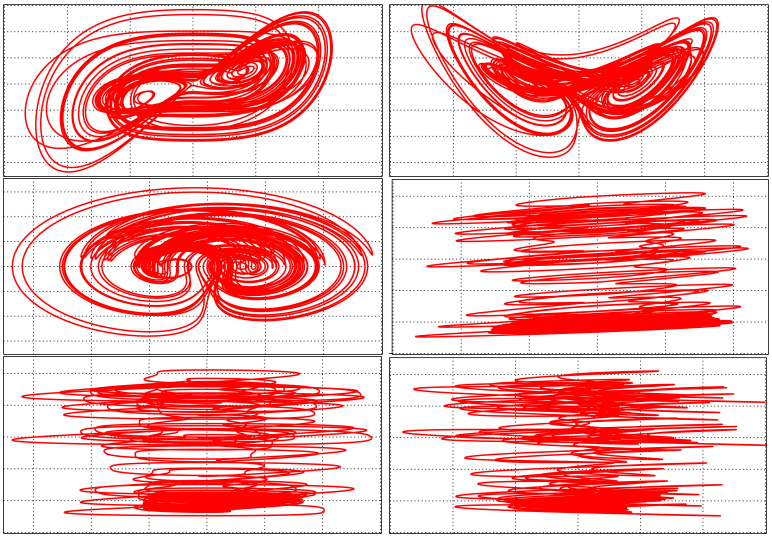


Figure 14. Phase portraits of circuit (4.4) implementing system (2.3) ($a = 5$, $b = 96$) as generated in Multisim oscilloscopes: a) $\widetilde{X}_1\widetilde{X}_2$, b) $\widetilde{X}_1\widetilde{X}_3$, c) $\widetilde{X}_2\widetilde{X}_3$, d) $\widetilde{X}_1\widetilde{X}_4$, e) $\widetilde{X}_2\widetilde{X}_4$, f) $\widetilde{X}_3\widetilde{X}_4$.

5. Chaotic attractors via fractal transformations based on the inverse Julia set

Fractal transformations based on Julia sets map the points of a sampled chaotic trajectory to new point sets with a multiplied, self-similar structure. We emphasize that these transformations are purely geometric: They act on the stored trajectory of system (2.3) after it has been computed, they do not modify the vector field, and they do not change any dynamical invariant of the system. They are therefore used here as a tool for generating structured patterns from the attractor, and the analysis below concerns the geometry of the transformed point sets, not the dynamics of system (2.3).

5.1. Application of the binary fractal transformation algorithm

To apply the binary fractal transformation to the chaotic attractor of system (2.3), we first select a two-dimensional projection of the numerically computed trajectory. For a given projection plane, two state variables of system (2.3) are relabeled for notational convenience. For example, for the (x_1, x_2) projection, we set:

$$x_n = x_1(t_n), \qquad y_n = x_2(t_n),$$

where $n = 1, 2, \ldots, k$ is a sample index enumerating the successive integration steps of the numerical solution. Analogously, for the (x_2, x_3) and (x_1, x_4) projections, one substitutes the corresponding pairs of state variables.

The binary fractal algorithm proposed by Bouallegue [26] is based on the inverse Julia map. Since the original description [26] is rather concise, we follow the systematic framework developed by Dai et al. [29]. The algorithm originates from the quadratic complex Z-map:

$$Z_{n+1} = Z_n^2 + Z_c. \tag{5.1}$$

Setting $Z_n = x_n + iy_n$, $Z_{n+1} = x_{n+1} + iy_{n+1}$, and $Z_c = 0$, we obtain the real and imaginary components:

$$\begin{cases} x_{n+1} = x_n^2 - y_n^2, \\ y_{n+1} = 2x_n y_n. \end{cases} \tag{5.2}$$

By exchanging subscripts in Eq (5.2), we derive the inverse transformation:

$$\begin{cases} x_n = x_{n+1}^2 - y_{n+1}^2, \\ y_n = 2x_{n+1} y_{n+1}. \end{cases} \tag{5.3}$$

Solving for x_{n+1} and y_{n+1} in terms of x_n and y_n yields the binary fractal transformation:

$$\begin{cases} x_{n+1} = \pm \sqrt{\dfrac{\pm \sqrt{x_n^2 + y_n^2} + x_n}{2}}, \\ y_{n+1} = \dfrac{y_n}{2x_{n+1}}, \end{cases} \tag{5.4}$$

where x_n and y_n are sequences generated by the chaotic system. In all cases, the sequences $\{x_n\}$ and $\{y_n\}$ represent discrete samples of the chosen projection of the attractor, and the binary fractal transformation (5.4) maps each input pair (x_n, y_n) to a transformed output pair (x_{n+1}, y_{n+1}) independently for each n. It should be emphasized that the subscript $n + 1$ in Eq (5.4) denotes the output of the transformation applied to the n-th sample, and does not refer to the next integration step of system (2.3). The $\pm$ signs in the transformation introduce branching that creates the fractal structure. At each iteration, the branch is selected randomly to populate the fractal attractor uniformly.

Following Bouallegue et al. [26], who introduced the term "Julia process fractal", we call the N-fold application of the inverse Julia map (5.4) to the sampled trajectory the *Julia process of order N*; the cases $N = 1, 2, 3$ are shown below. In the Julia process, each iteration doubles the number of structural components, so that their number grows geometrically, $M_2 = M_1 \cdot 2^N$ (see Eq (5.7) below). This should be distinguished from the Julia transformation technique [57–59], in which the number of fractal wings grows linearly with the order of the transformation ($2k$ wings for $n = k$).

We apply the binary fractal transformation to our four-dimensional chaotic system (2.3) with parameters $a = 5$ and $b = 96$. The system is chaotic with Lyapunov exponents $LE_i = (0.7859, 0.0007, -0.0017, -5.7849)$ (Table 2). The original system was integrated using the fourth-order Runge–Kutta method with the initial conditions $\mathbf{x}_0 = [5, 10, 5, 5]^T$ over the time interval $t \in [0, 300]$. For the fractal transformation, we selected different pairs of state variables from the steady-state portion of the trajectory (discarding the initial transient to avoid transitional effects). The results of applying the binary fractal algorithm to various projections of the chaotic attractor are presented in Figures 15–17.

Figure 15 shows the fractal transformation applied to the (x_1, x_2) projection of the phase space. The original chaotic attractor displays a characteristic double-lobe butterfly-like structure. After a single fractal transformation (Figure 15(a)), the attractor reorganizes into two symmetrically distributed regions with enhanced geometric complexity, forming an X-shaped pattern. The double transformation (Figure 15(b)) produces four distinct lobes arranged in a star-like configuration with increased spatial coverage and finer structural details. After triple transformation (Figure 15(c)), eight regions emerge, creating a highly intricate fractal structure with self-similar features at multiple scales.

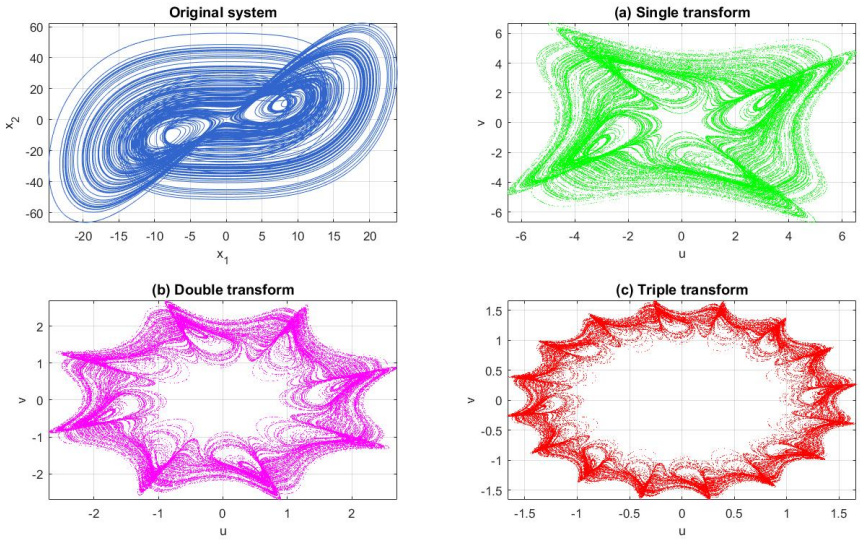


Figure 15. Binary Julia process applied to the (x_1, x_2) projection of the attractor of system (2.3) ($a = 5$, $b = 96$): original attractor (top left), (a) $N = 1$ (top right), (b) $N = 2$ (bottom left), and (c) $N = 3$ (bottom right). The original double-lobe structure evolves into 2, 4, and 8 symmetrically distributed regions.

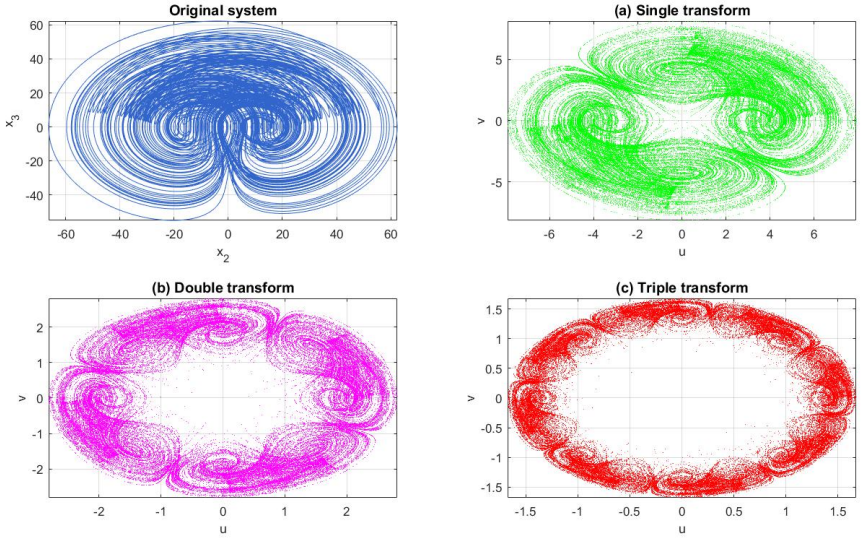


Figure 16. Binary Julia process applied to the (x_2, x_3) projection of the attractor of system (2.3) ($a = 5$, $b = 96$): original attractor (top left), (a) $N = 1$ (top right), (b) $N = 2$ (bottom left), and (c) $N = 3$ (bottom right). The circular attractor topology is preserved while the number of structures doubles with each transformation.

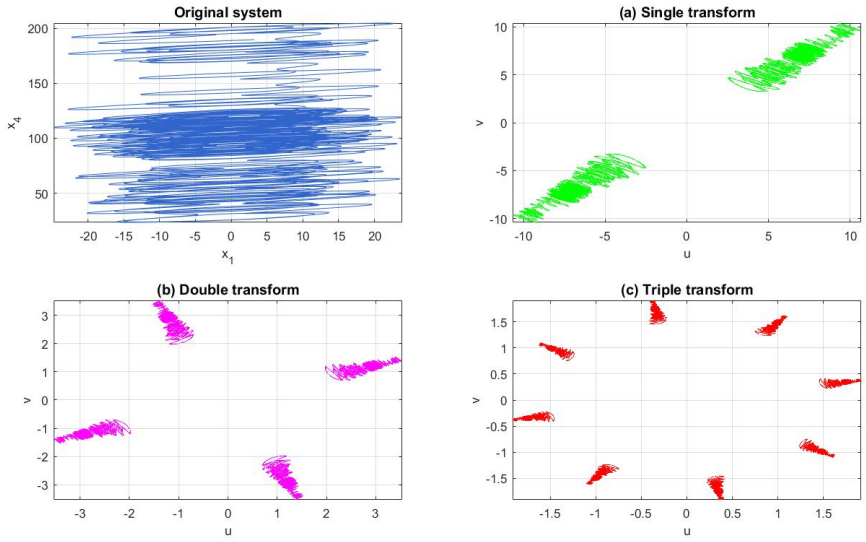


Figure 17. Binary Julia process applied to the (x_1, x_4) projection of the attractor of system (2.3) ($a = 5$, $b = 96$): original attractor (top left), (a) $N = 1$ (top right), (b) $N = 2$ (bottom left), and (c) $N = 3$ (bottom right). The band-like chaotic attractor fragments into separated clusters following the power growth law $M_2 = M_1 \times 2^N$.

The (x_2, x_3) projection, shown in Figure 16, reveals a different aspect of the system's dynamics. The original attractor exhibits a circular ring-like structure with dual spiral centers. The single transformation (Figure 16(a)) maintains the overall circular topology while creating two symmetric spiraling regions. With double transformation (Figure 16(b)), four spiral structures emerge around the periphery, and the triple transformation (Figure 16(c)) produces eight distinct spiral patterns, demonstrating the preservation of local dynamical features during the fractal replication process.

Figure 17 presents the transformation results for the (x_1, x_4) projection, where the original system displays a broad band-like chaotic attractor with multiple horizontal layers. This projection demonstrates particularly interesting behavior under fractal transformation. The single transformation (Figure 17(a)) splits the continuous band into two distinct diagonal clusters. The double transformation (Figure 17(b)) further fragments the attractor into four separated regions located in different quadrants of the phase plane. After triple transformation (Figure 17(c)), eight compact clusters appear, distributed across the phase space in a highly organized manner.

The structural doubling observed in Figures 15–17 can be explained by the structure of the inverse Julia map. Writing the forward quadratic map $z \mapsto z^2$ (the case $c = 0$ underlying (5.4)) in real coordinates $z = x + iy$ as $f(x, y) = (x^2 - y^2,\ 2xy)$, its Jacobian matrix and determinant are

$$Df(x, y) = \begin{pmatrix} 2x & -2y \\ 2y & 2x \end{pmatrix}, \qquad \det Df(x, y) = 4(x^2 + y^2) = 4\,|z|^2. \tag{5.5}$$

The determinant vanishes only at the single critical point $z = 0$, and $\det Df > 0$ everywhere else. Hence, away from the origin, f is an orientation-preserving local diffeomorphism, and by the inverse function theorem, each point (x_n, y_n) possesses a well-defined local inverse. Globally, however, f is a two-to-one map: Since $f(z) = f(-z)$, every $z_n \neq 0$ has exactly two distinct preimages, $\pm\sqrt{z_n}$, which

are exchanged by the sign of the outer radical in

$$x_{n+1} = \pm\sqrt{\frac{\sqrt{x_n^2+y_n^2}+x_n}{2}}, \qquad y_{n+1} = \frac{y_n}{2x_{n+1}}. \tag{5.6}$$

Only the "+" sign of the inner square root is admissible, since $\sqrt{x_n^2+y_n^2}+x_n \geq 0$; the outer sign generates the two preimages $\pm\sqrt{z_n}$, which are related by the point reflection $w \mapsto -w$. The Jacobian argument is local: It shows that each branch is a local diffeomorphism away from the origin, but it does not determine how the two branches are arranged globally. The global structure is described by the following statement.

Proposition 1. *Let $K \subset \mathbb{C}\setminus\{0\}$ and let $S_N = \{w \in \mathbb{C} : \ w^{2^N} \in K\}$ be the set obtained from K by N applications of the inverse map* (5.6) *with all possible branch choices. Set $\omega_N = e^{2\pi i/2^N}$ and $\Theta_N = \{w \neq 0 : \ 0 \leq \arg w < 2\pi/2^N\}$. Then*

(i) $\omega_N S_N = S_N$, i.e., S_N has exact 2^N-fold rotational symmetry about the origin;
(ii) $S_N = \bigcup_{k=0}^{2^N-1} \omega_N^k F_N$ with $F_N = S_N \cap \Theta_N$, where the 2^N sets $\omega_N^k F_N$ are pairwise disjoint and congruent (they are obtained from each other by rotations), and each of them is mapped one-to-one onto K by $w \mapsto w^{2^N}$.

Proof. If $w \in S_N$, then $(\omega_N^k w)^{2^N} = \omega_N^{k2^N} w^{2^N} = w^{2^N} \in K$, which proves (i). The sectors $\omega_N^k\Theta_N$, $k = 0,\ldots,2^N-1$, form a partition of $\mathbb{C}\setminus\{0\}$; hence, by (i), $S_N = \bigcup_k (S_N \cap \omega_N^k\Theta_N) = \bigcup_k \omega_N^k F_N$, and the sets in this union are pairwise disjoint. Finally, $w \mapsto w^{2^N}$ multiplies $\arg w$ by 2^N and raises $|w|$ to the power 2^N; it therefore maps Θ_N bijectively onto $\mathbb{C}\setminus\{0\}$, and hence maps F_N bijectively onto K. □

Thus N applications of the inverse Julia map produce 2^N congruent copies of the original structure, arranged with exact 2^N-fold rotational symmetry. If the original projection consists of M_1 distinguishable structures (lobes or scrolls), the transformed set contains

$$M_2 = M_1 \times 2^N \tag{5.7}$$

congruent structures. This is the power law observed in Figures 15–17 for $N = 1, 2, 3$. In the numerical algorithm, the random choice of the outer sign at each iteration assigns every point to one of the 2^N copies with probability 2^{-N}, so that all copies are populated uniformly.

Remark 1. *Proposition 1 concerns congruent copies, not connected components. The copies $\omega_N^k F_N$ are disjoint, but their closures may touch along the boundary rays of the sectors. If K does not intersect some ray $\ell = \{re^{i\theta} : \ r \geq 0\}$, the sectors can be chosen as $\{\theta/2^N \leq \arg w < (\theta+2\pi)/2^N\}$ and its rotations, whose boundary rays are mapped into ℓ; then S_N does not meet these rays, each copy is homeomorphic to K, and every connected component of K gives rise to exactly 2^N connected components of S_N. If, however, K surrounds the origin, the copies are glued together along the boundary rays and S_N may be connected; for example, the preimage of the unit circle under $z \mapsto z^2$ is the unit circle itself. The projections of the attractor of system* (2.3) *belong to the second case: for instance, the projected trajectory in the (x_1, x_2) plane winds about* 140 *times around the origin over the time interval used. Therefore the transformed sets in Figures 15–17 are, in general, connected (cf. the connected star-like patterns in Figure 15), and the numbers* 2, 4, *and* 8 *refer to the congruent structures described by Proposition 1, not to connected components.*

Here, M_1 is the number of connected components of the original attractor projection, N is the number of transformations, and M_2 is the resulting number of structures. For the cases presented:

- Julia process of order $N = 1$: $M_2 = 1 \times 2^1 = 2$ structures;
- Julia process of order $N = 2$: $M_2 = 1 \times 2^2 = 4$ structures;
- Julia process of order $N = 3$: $M_2 = 1 \times 2^3 = 8$ structures.

The fractal transformation preserves the fundamental chaotic nature of the system while substantially increasing its geometric complexity and spatial distribution. Each successive transformation maintains self-similarity at different scales, a hallmark of fractal geometry. The randomness introduced by the $\pm$ branch selection in Eq (5.4) ensures that all fractal lobes are populated during numerical simulation.

Notably, different phase space projections reveal distinct geometric patterns under transformation: the (x_1, x_2) projection produces connected star-like patterns, the (x_2, x_3) projection maintains circular spiral structures, while the (x_1, x_4) projection generates separated clusters. This diversity demonstrates that the fractal transformation interacts differently with various dynamical features of the chaotic system, reflecting the different positions of the projected attractors relative to the origin.

The transformation distributes the attractor more uniformly in phase space while maintaining the essential chaotic dynamics, as confirmed by the positive Lyapunov exponent of the underlying system.

5.2. Application of ternary fractal transformation algorithm

The binary fractal algorithm operates on two-dimensional sequences, which limits its application to planar projections of higher-dimensional chaotic systems. To overcome this limitation and enable fractal transformations in three-dimensional space, we develop an extended ternary fractal algorithm. This extension is particularly valuable for chaotic systems naturally evolving in three or more dimensions, as it preserves the volumetric structure of the phase space during transformation.

The derivation follows a similar mathematical framework to the binary case, but utilizes a three-component hypercomplex representation. We introduce a ternary number of the form $P = a + ib + jc$, where i and j are hypercomplex units satisfying $i^2 = j^2 = -1$. The key question is how to define the product ij.

While the original work [29] introduced a ternary number system with $ij = 0$, here we consider the alternative commutative multiplication rule $ij = ji = -1$. Both rules define commutative but non-associative algebras and are not related to the quaternions, in which $ij = k = -ji$; their algebraic structure and its consequences are discussed in Remark 3. Under the rule $ij = ji = -1$, the forward transformation from the Julia map $Z_{n+1} = Z_n^2$ yields:

$$\begin{cases} x_{n+1} = x_n^2 - y_n^2 - z_n^2 - 2y_n z_n, \\ y_{n+1} = 2x_n y_n, \\ z_{n+1} = 2x_n z_n. \end{cases} \tag{5.8}$$

Next, we exchange the position of variables in Eq (5.8) to obtain the inverse relationship:

$$\begin{cases} x_n = x_{n+1}^2 - y_{n+1}^2 - z_{n+1}^2 - 2y_{n+1} z_{n+1}, \\ y_n = 2x_{n+1} y_{n+1}, \\ z_n = 2x_{n+1} z_{n+1}. \end{cases} \tag{5.9}$$

From the second and third equations of (5.9), we can express:

$$y_{n+1} = \frac{y_n}{2x_{n+1}}, \quad z_{n+1} = \frac{z_n}{2x_{n+1}}.$$

Substituting these into the first equation, we obtain a biquadratic equation for x_{n+1}, whose solution is derived in Proposition 2 below:

$$\begin{cases} x_{n+1} = \pm\sqrt{\dfrac{\sqrt{x_n^2 + (y_n + z_n)^2} + x_n}{2}}, \\ y_{n+1} = \dfrac{y_n}{2x_{n+1}}, \\ z_{n+1} = \dfrac{z_n}{2x_{n+1}}. \end{cases} \tag{5.10}$$

This constitutes the ternary fractal transformation. The ± sign in the expression for x_{n+1} creates branching at each iteration, analogous to the binary case, but now operating in three-dimensional space. The three sequences x_n, y_n, and z_n are obtained from the numerical solution of the chaotic system, and the transformation can be applied iteratively to generate increasingly complex fractal structures.

By Proposition 2, every point outside a singular set Σ_{-1} has exactly two preimages; therefore, as in the binary case, each application of the ternary transformation doubles the number of points, and the numerical results below show the corresponding doubling of structural components. For $N = 1$, the preimage set is invariant under the point reflection $(u, v, w) \mapsto (-u, -v, -w)$ for both rules. For the rule $ij = -1$, the map acts as complex squaring on $x + i(y + z)$ (Remark 2); hence Proposition 1 applies to the projection onto the plane $(u,\ v + w)$, which has exact 2^N-fold rotational symmetry. However, the ternary version preserves the three-dimensional geometry of the original system, enabling visualization of fractal transformations in the full phase space rather than restricting to planar projections.

The ternary fractal transformation defined by Eq (5.10) was applied to the three-dimensional chaotic attractor obtained from the system, namely, to the variables (x_1, x_2, x_3) of system (2.3) ($a = 5$, $b = 96$, initial conditions (3.5)), integrated over $t \in [0, 300]$ with the first half of the trajectory discarded as transient. Each variable was standardized as $\tilde{x}_k = (x_k - \langle x_k \rangle)/(3\, s_k)$, where $\langle x_k \rangle$ and s_k are its mean and standard deviation, so that the normalized data lie approximately in $[-1, 1]$; the triples $(\tilde{x}_1, \tilde{x}_2, \tilde{x}_3)$ serve as (x_n, y_n, z_n) in Eq (5.10). The transformation was performed iteratively up to three times ($N = 1, 2, 3$), generating increasingly complex fractal structures. The results are presented through multiple projection views (Figures 18–21) to fully characterize the three-dimensional geometry. In our computations, the inner sign in the expression for x_{n+1} was also chosen at random. By Proposition 2, the choice "−" gives a non-positive argument of the outer square root, so these draws have no real image and were discarded; this explains why only 49.8%, 24.8%, and 12.3% of the 95, 844 input points were retained after $N = 1, 2, 3$ iterations, respectively (approximately 2^{-N}). The retained points are exactly the images under the admissible branches, so the geometry of the structures in Figures 18–21 is not affected; only the point density is reduced. With the inner sign fixed to "+", as in Eqs (5.10) and (5.11), no points are lost, except for points close to the singular set Σ_{-1}, where $|x_{n+1}|$ is small and $|y_{n+1}|, |z_{n+1}|$ become very large. In the computations, points with $|x_{n+1}| \le 10^{-3}$ or $\max(|y_{n+1}|, |z_{n+1}|) \ge 10$ are removed; with the admissible branch, this cut-off removes less than 1% of the points per iteration: of the 95, 844 input points, 99.3%, 98.7%, and 98.2% are retained after $N = 1, 2, 3$, respectively. For the rule $ij = 0$, whose singular set Σ_0 is only a half-line, no points are removed at all.

5.2.1. Projection (u, v)

Figure 18 illustrates the projection onto the (u, v) plane, which reveals the horizontal structure of the transformed attractors. The single transformation (panel (a)) exhibits a characteristic multi-lobed pattern with four primary regions of high point density arranged in a cross-like configuration. The central vertical structure at $u \approx 0$ indicates a concentration of trajectories passing through the transformation's critical manifold.

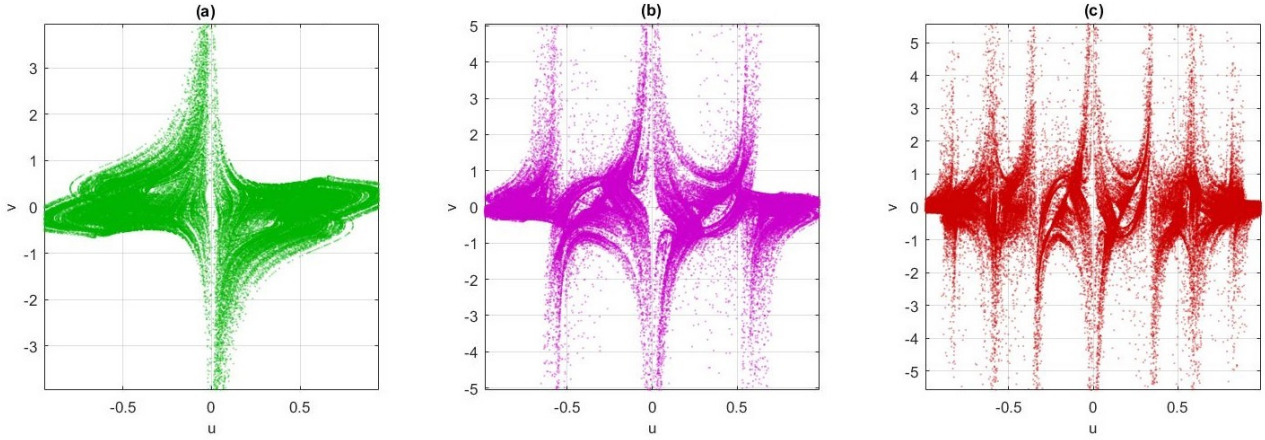


Figure 18. Projection of the ternary fractal transformation onto the (u, v) plane. Attractor of system (2.3) ($a = 5$, $b = 96$), $ij = -1$: (a) $N = 1$ (95,187 points, 99.3%); (b) $N = 2$ (94,603 points, 98.7%); (c) $N = 3$ (94,137 points, 98.2%). The progressive doubling of structural components is clearly visible, with each iteration creating bifurcations in the existing lobes while maintaining four-fold symmetry.

The double transformation (Figure 18(b)) demonstrates a clear bifurcation of each lobe present in the single transformation, consistent with the theoretical prediction that each iteration doubles the number of structural components. The symmetry of the pattern reflects the ± sign choices in Eq (5.10), which create mirror images in the u coordinate. Additionally, the increased dispersion along the v axis indicates that the second transformation amplifies variations in the y component relative to x.

The triple transformation (Figure 18(c)) shows further structural multiplication, with each of the four lobes from the double transformation splitting into two distinct components. However, the reduced point density (12.3% retention) causes some regions to appear sparser, particularly at the periphery of the attractor. The overall structure maintains the four-fold symmetry, while each primary lobe develops internal sub-lobes at smaller scales, geometrically similar to the primary ones, reflecting the self-similar hierarchy introduced by successive applications of the branching transformation.

5.2.2. Projection (u, w)

Figure 19 presents the projection onto the (u, w) plane, providing complementary information about the vertical organization of the fractal structures. Similar to the (u, v) projection, the single transformation (Figure 19(a)) displays four primary lobes arranged around the vertical axis at $u \approx 0$. The distribution along the w axis follows a similar pattern to that along the v axis, which is expected given the symmetric roles of the y and z components in Eq (5.10).

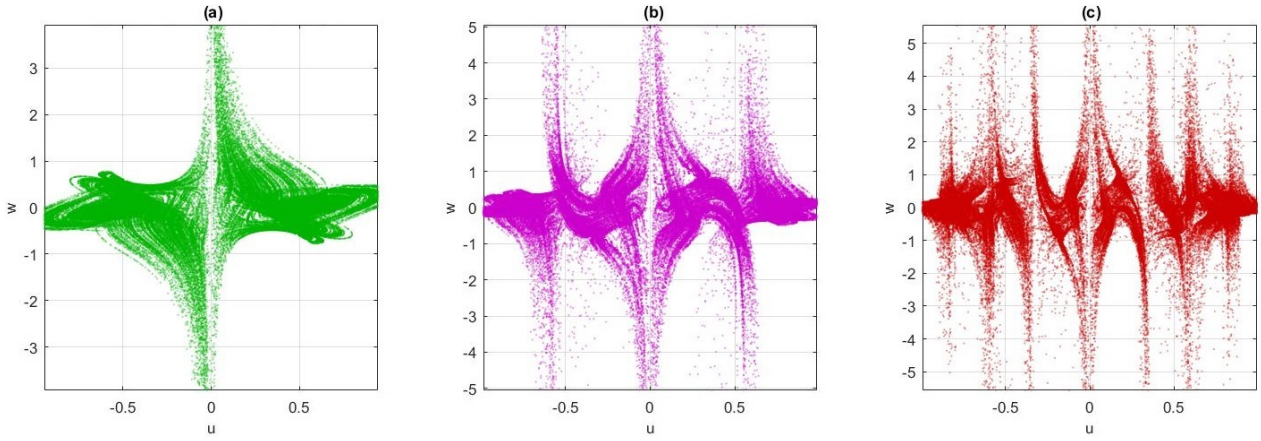


Figure 19. Projection of the ternary fractal transformation onto the (u, w) plane, attractor of system (2.3) ($a = 5$, $b = 96$), $ij = -1$: (a) $N = 1$ (95,187 points, 99.3%); (b) $N = 2$ (94,603 points, 98.7%); (c) $N = 3$ (94,137 points, 98.2%). The vertical structure mirrors the horizontal patterns observed in Figure 18, confirming the symmetric treatment of the x and z components in the transformation algorithm. Progressive bifurcation and increased vertical spread are evident with each iteration.

The progression from single to double (Figure 19(b)) and triple (Figure 19(c)) transformations again shows the systematic doubling of structural elements. Each lobe in Figure 19(a) bifurcates into two distinct components in Figure 19(b), and these further split in Figure 19(c). The vertical spread increases with iteration number, indicating that successive transformations amplify the z component variations relative to the x component, consistent with the division by $2x_{n+1}$ in the transformation formula.

5.2.3. Projection (v, w)

Figure 20 depicts the projection onto the (v, w) plane, which eliminates the u coordinate and reveals the transverse structure of the transformed attractors. Unlike the (u, v) and (u, w) projections that showed four-lobed patterns, the (v, w) projection displays a fundamentally different geometry: a diagonal band structure extending from the upper-left to the lower-right quadrant.

This diagonal pattern arises because the v and w components are both inversely proportional to x_{n+1} in Eq (5.10), establishing a correlation between these two coordinates. The width of the diagonal band reflects the variability in the ratio y_n/z_n from the original attractor. The single transformation (Figure 20(a)) shows a relatively dense diagonal structure, while the double and triple transformations (Figure 20(b),(c)) exhibit a doubling of the band width and the emergence of parallel diagonal striations.

The progression through successive transformations demonstrates that while the overall diagonal alignment is preserved, the internal structure becomes increasingly complex. The triple transformation (Figure 20(c)) shows multiple parallel diagonal bands, each corresponding to a different branch of the nested square-root operations. The reduced point density in higher-order transformations makes individual branches more distinguishable, revealing the hierarchical fractal organization.

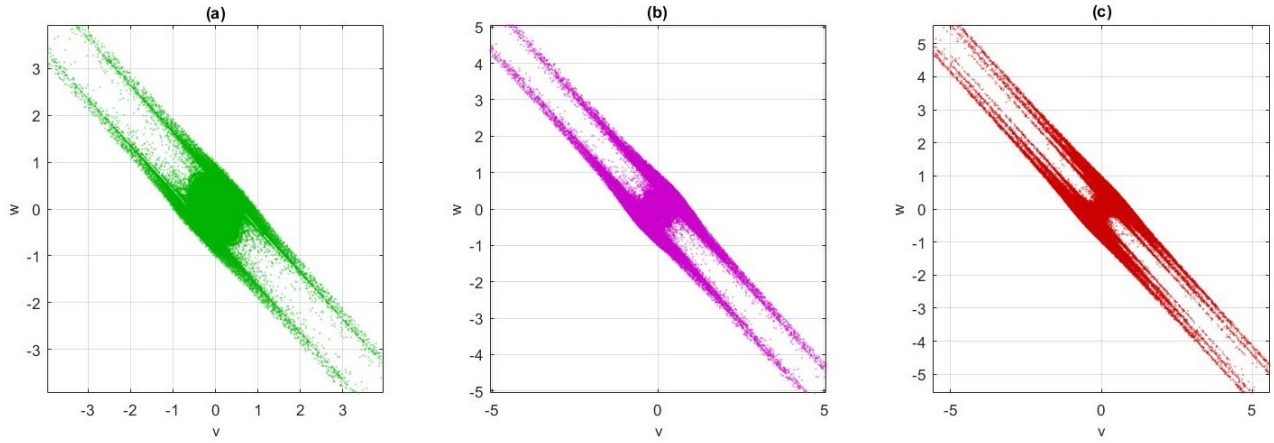


Figure 20. Projection of the ternary fractal transformation onto the (v, w) plane, attractor of system (2.3) ($a = 5$, $b = 96$), $ij = -1$: (a) $N = 1$ (95,187 points, 99.3%), showing a dense diagonal band structure; (b) $N = 2$ (94,603 points, 98.7%), exhibiting band widening and parallel striations; (c) $N = 3$ (94,137 points, 98.2%), revealing multiple parallel diagonal components. The diagonal alignment arises from the correlation between v and w components, both of which are inversely proportional to x_{n+1} in Eq (5.10). This projection uniquely captures the fractal organization in the transverse plane.

5.2.4. Three-dimensional structure

Figure 21 presents the full three-dimensional visualization of the transformed attractors in (u, v, w) space. To maintain visual clarity, only a representative subset of points is displayed (approximately 5000–6000 points per panel). The single transformation (Figure 21(a)) reveals a twisted ribbon-like structure with multiple layers, combining the four-lobed pattern observed in the (u, v) and (u, w) projections with the diagonal correlation between v and w.

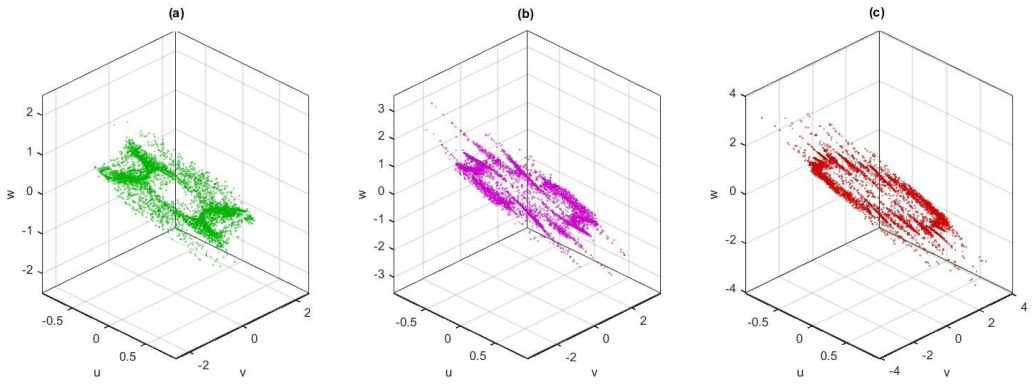


Figure 21. Three-dimensional visualization of the ternary fractal transformation in (u, v, w) space, attractor of system (2.3) ($a = 5$, $b = 96$), $ij = -1$: (a) $N = 1$ (5010 of 95,187 points); (b) $N = 2$ (5256 of 94,603 points); (c) $N = 3$ (5230 of 94,137 points). The fractal nature of the structure is evident in the self-similar patterns at different scales.

The double transformation (Figure 21(b)) shows a more complex structure with additional layers

and finer detail. Each ribbon from the single transformation has split into two parallel sheets, and the overall volume occupied by the attractor has expanded. The triple transformation (Figure 21(c)) continues this trend, with further subdivision of the ribbon structure and increased geometric complexity. The self-similar nature of the fractal is evident in the repeating patterns at different scales.

The Lyapunov exponents of system (2.3) are not affected by the fractal transformation, since they characterize the dynamics of the flow rather than the geometry of any particular projection. The transformation reorganizes the spatial distribution of the attractor points while leaving the underlying chaotic dynamics unchanged. The branching inherent in the signs of Eq (5.10) creates a multi-layered structure that fills the three-dimensional phase space more efficiently than the original attractor, consistent with the increase in fractal dimension typically associated with such transformations.

5.2.5. Comparison with $ij = 0$ formulation

To assess the impact of the hypercomplex multiplication rule, we compare our results obtained with $ij = -1$ (Figures 18–21) with those generated using the original formulation $ij = 0$ from [29]. The alternative transformation equations with $ij = 0$ yield:

$$\begin{cases} x_{n+1} = \pm\sqrt{\dfrac{\sqrt{x_n^2 + y_n^2 + z_n^2} + x_n}{2}}, \\ y_{n+1} = \dfrac{y_n}{2x_{n+1}}, \\ z_{n+1} = \dfrac{z_n}{2x_{n+1}}. \end{cases} \tag{5.11}$$

The key difference lies in the radial term: $(y_n + z_n)^2$ for $ij = -1$ versus $y_n^2 + z_n^2$ for $ij = 0$.

Both inverse formulas (5.10) and (5.11) follow from the same argument, which we now give in full.

Proposition 2. *Let $P = x + iy + jz$ with $i^2 = j^2 = -1$ and $ij = ji = \mu$, $\mu \in \{-1, 0\}$, and let $F_\mu(x, y, z)$ denote the components of P^2:*

$$F_{-1} : (x, y, z) \mapsto (x^2 - (y + z)^2,\ 2xy,\ 2xz), \qquad F_0 : (x, y, z) \mapsto (x^2 - y^2 - z^2,\ 2xy,\ 2xz).$$

Set $\rho_{-1}(y, z) = y + z$, $\rho_0(y, z) = \sqrt{y^2 + z^2}$ and $\Sigma_\mu = \{(x, y, z) : \rho_\mu(y, z) = 0,\ x \le 0\}$. Then for every $(x_n, y_n, z_n) \notin \Sigma_\mu$, the equation $F_\mu(X, Y, Z) = (x_n, y_n, z_n)$ has exactly two real solutions,

$$X = \pm\sqrt{\frac{x_n + \sqrt{x_n^2 + \rho_\mu(y_n, z_n)^2}}{2}}, \qquad Y = \frac{y_n}{2X}, \qquad Z = \frac{z_n}{2X}, \tag{5.12}$$

which coincide with Eq (5.10) for $\mu = -1$ and with Eq (5.11) for $\mu = 0$. Only the "+" sign of the inner square root is admissible.

Proof. If $X = 0$, then $y_n = 2XY = 0$, $z_n = 2XZ = 0$, and $x_n = -\rho_\mu(Y, Z)^2 \le 0$, i.e., $(x_n, y_n, z_n) \in \Sigma_\mu$. Hence, for Σ_μ, every solution has $X \neq 0$, and the last two equations give $Y = y_n/(2X)$ and $Z = z_n/(2X)$ uniquely. For both rules, $\rho_\mu(Y, Z)^2 = \rho_\mu(y_n, z_n)^2/(4X^2)$: for $\mu = -1$, $(Y + Z)^2 = (y_n + z_n)^2/(4X^2)$, and for $\mu = 0$, $Y^2 + Z^2 = (y_n^2 + z_n^2)/(4X^2)$. With $\rho_n := \rho_\mu(y_n, z_n)$, the first component of F_μ therefore yields

$$x_n = X^2 - \frac{\rho_n^2}{4X^2} \quad \Longleftrightarrow \quad 4X^4 - 4x_nX^2 - \rho_n^2 = 0,$$

a quadratic equation in X^2 with roots $X^2 = \frac{1}{2}(x_n \pm \sqrt{x_n^2 + \rho_n^2})$. The root with "−" is non-positive and could only give $X = 0$, which is excluded; the root with "+" is strictly positive Σ_μ. This gives the two values of X in (5.12), and direct substitution shows that both are solutions. □

Remark 2. *Proposition 2 explains the geometry of the two rules. For $\mu = -1$, with $s = y + z$, the map F_{-1} acts as the complex squaring $x+is \mapsto (x+is)^2$ and preserves the ratio $y : z$; hence the transformed points are distributed along rays through the origin of the (v, w) plane, which produces the diagonal bands in Figure 20. For $\mu = 0$, writing $(y, z) = r(\cos\theta, \sin\theta)$, the map F_0 acts as $x + ir \mapsto (x + ir)^2$ and preserves θ, i.e., it commutes with rotations about the x axis; this rotational symmetry produces the concentric patterns in Figure 22. The Jacobian determinants are* $\det DF_{-1} = 8x(x^2 + (y + z)^2)$ *and* $\det DF_0 = 8x(x^2 + y^2 + z^2)$*; both vanish on the plane $x = 0$, which separates the two inverse branches ($X > 0$ and $X < 0$). The singular set Σ_{-1} is a half-plane, whereas Σ_0 is only a half-line.*

Remark 3 (Algebraic structure of the ternary rules)**.** *Let $\mathcal{A}_\mu$ denote $\mathbb{R}^3$ with basis $\{1, i, j\}$ and the bilinear commutative product defined by $i^2 = j^2 = -1$, $ij = ji = \mu$. Neither $\mathcal{A}_{-1}$ nor $\mathcal{A}_0$ is a division algebra, and no choice of the product could make it one: by the theorem of Bott, Milnor, and Kervaire, finite-dimensional real division algebras (associative or not) exist only in dimensions* $1, 2, 4,$ *and* 8*. Both algebras are commutative but not associative (e.g., $(ii)j = -j$, whereas $i(ij) = \mu i$), both contain zero divisors: $ij = 0$ in $\mathcal{A}_0$, and $e = j - i$ satisfies $e^2 = 0$, and $ie = 0$ in $\mathcal{A}_{-1}$. These properties affect the transformations in three ways. (i) The transformations use only the square $P \mapsto P^2 = P \cdot P$, which is well-defined in any algebra; non-associativity therefore plays no role for the quadratic map, but higher powers P^k, $k \geq 3$, would depend on the bracketing, so only the quadratic Julia process has an unambiguous ternary analogue. (ii) The zero divisors make the squaring map non-surjective: points of the singular sets Σ_μ of Proposition 2 have no real preimage, and near Σ_{-1} (a half-plane) the preimages become unbounded, which is the origin of the small loss of points for $ij = -1$; for $ij = 0$, the singular set is only a half-line and no points are lost. (iii) The algebraic structure determines the geometry of the results. In the basis $\{1, i, e\}$, $P = x + (y + z)\,i + z\,e$ and $P^2 = (x + si)^2 + 2xz\,e$ with $s = y + z$, i.e., $\mathcal{A}_{-1}$ acts as complex squaring on $x + is$ together with a linear scaling of the nilpotent coordinate; this produces the anisotropic, essentially two-dimensional ribbon structures of Figures 18–21. In $\mathcal{A}_0$, every plane* $\mathrm{span}\{1, u\}$ *with $u = (yi + zj)/r$, $r = \sqrt{y^2 + z^2}$, is a subalgebra isomorphic to $\mathbb{C}$ ($u^2 = -1$), so $\mathcal{A}_0$ is a fan of complex planes sharing the real axis; squaring preserves each plane, which produces the rotational symmetry and the isotropic, torus-like structures of Figures 22–23. Thus the ternary transformations are well-defined despite the algebraic deficiencies, and the differences between the two rules observed in Section 5 are direct consequences of these deficiencies.*

Figures 22–23 present the corresponding projections obtained with the $ij = 0$ formulation. Several notable geometric differences emerge.

The most pronounced difference appears in the (v, w) projection (Figure 22). While the $ij = -1$ case produces diagonal bands due to the correlation term $2y_nz_n$, the $ij = 0$ formulation generates concentric circular patterns. As shown in Remark 2, this arises because the transformation with $ij = 0$ commutes with rotations about the x axis, whereas for $ij = -1$, the term $\sqrt{x_n^2 + (y_n + z_n)^2}$ couples the y and z components along the direction $y + z$ and breaks this rotational symmetry.

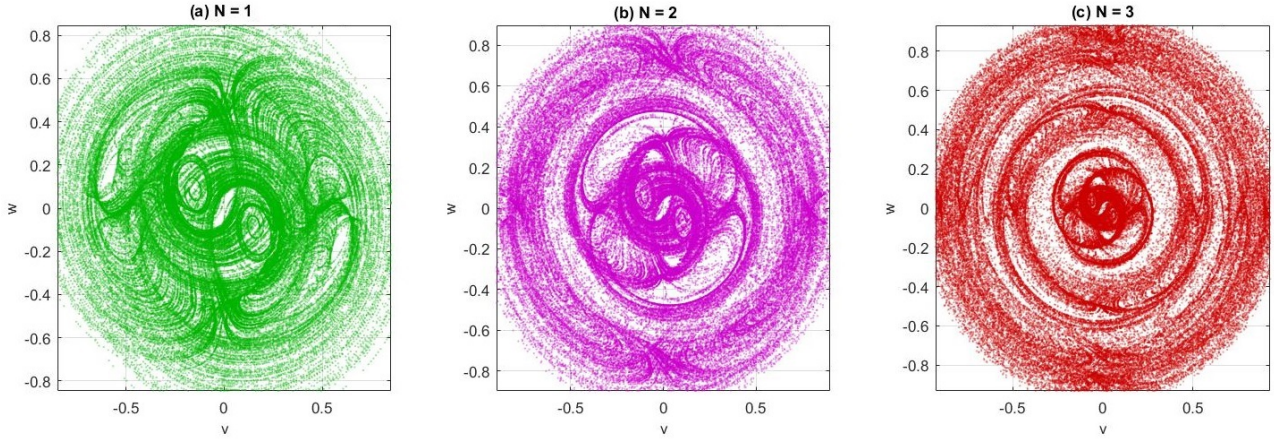


Figure 22. Projection onto the (v, w) plane using $ij = 0$, attractor of system (2.3) ($a = 5$, $b = 96$). In contrast to the diagonal band structure in Figure 20, this formulation generates concentric circular patterns. The single transformation (a) shows nested spiral structures, while successive transformations (b)-(c) create multiple concentric rings.

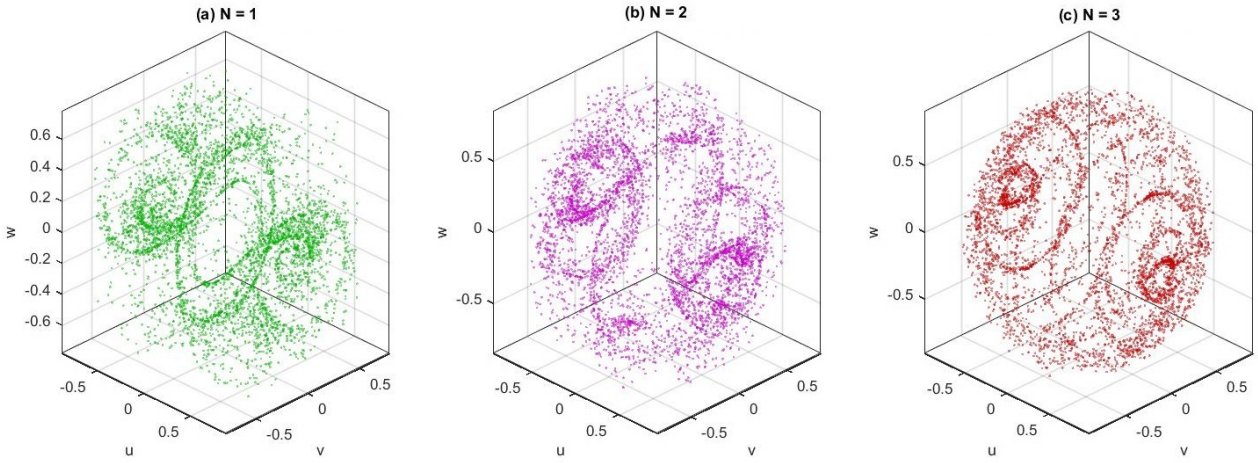


Figure 23. Three-dimensional visualization using $ij = 0$, attractor of system (2.3) ($a = 5$, $b = 96$). The structure exhibits a spiral torus-like geometry with circular cross-sections in the (v, w) plane, fundamentally different from the twisted ribbon structure observed with $ij = -1$ (Figure 21).

The (u, v) and (u, w) projections (Figures 24 and 25) reveal a two-lobed structure with the $ij = 0$ formulation, contrasting with the four-lobed pattern observed with $ij = -1$. Since both rules yield exactly two preimages per point (Proposition 2), this difference is geometric rather than combinatorial: it reflects the different symmetries of the two transformations (Remark 2). The bilateral symmetry about the v and w axes in the $ij = 0$ case is a direct consequence of treating y and z independently.

The three-dimensional visualization (Figure 23) shows that the $ij = 0$ formulation produces a spiral torus-like structure with approximately circular cross-sections, consistent with the concentric patterns in the (v, w) projection. This contrasts sharply with the multi-layered ribbon geometry of the $ij = -1$ case, which exhibits anisotropic stretching along the diagonal direction in the (v, w) plane.

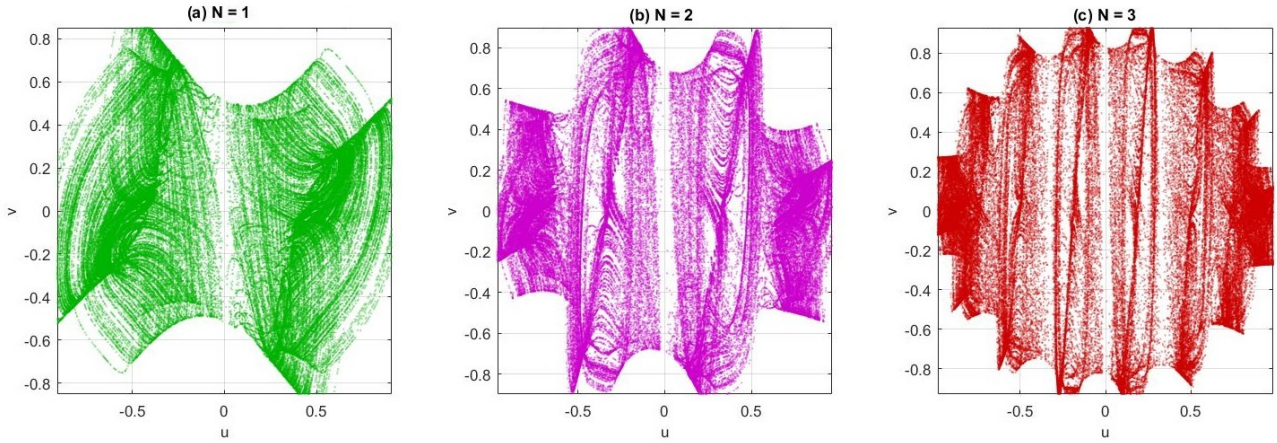


Figure 24. Projection onto the (u, v) plane using the ternary fractal transformation with $ij = 0$ [29], attractor of system (2.3) ($a = 5$, $b = 96$). (a) $N = 1$; (b) $N = 2$; (c) $N = 3$. Compared to Figure 18, this formulation produces a two-lobed rather than four-lobed structure, with pronounced bilateral symmetry about the v axis. Both rules yield two preimages per point; the difference in the number of lobes reflects their different symmetries (Remark 2).

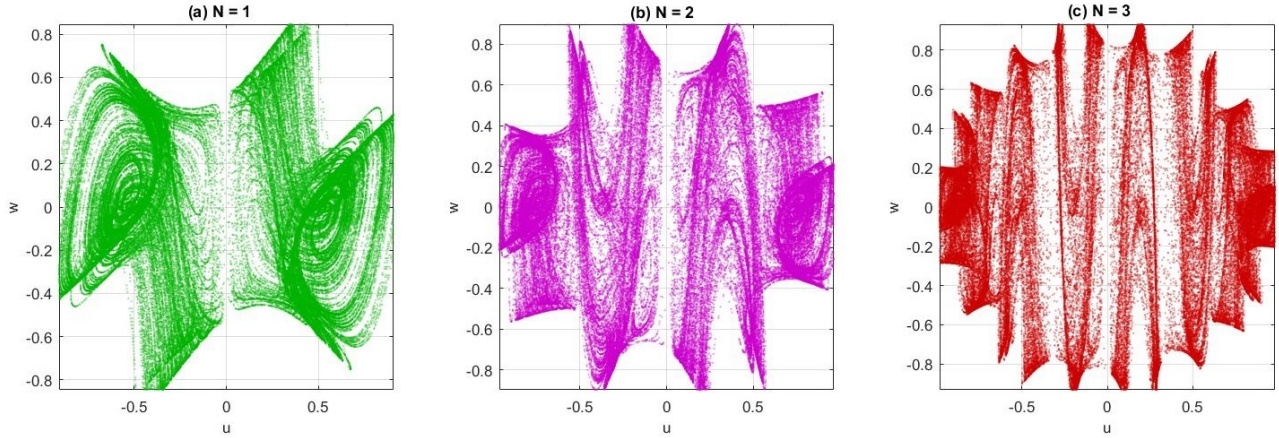


Figure 25. Projection onto the (u, w) plane using $ij = 0$, attractor of system (2.3) ($a = 5$, $b = 96$). The structure mirrors that in Figure 24, with two primary lobes showing bilateral symmetry about the w axis. This symmetry pattern differs fundamentally from the four-lobed configuration observed with $ij = -1$ (Figure 19).

From a mathematical perspective, neither rule is algebraically preferable: both define commutative, non-associative algebras (for $ij = -1$, the element $j - i$ is even nilpotent, $(j - i)^2 = 0$). The $ij = 0$ formulation has the additional rotational symmetry about the x axis and a smaller singular set. The geometric consequences are significant: $ij = -1$ generates anisotropic fractal structures with preferential directions, while $ij = 0$ produces more isotropic patterns with rotational symmetry about the x axis. Both formulations successfully generate complex fractal attractors through iterative transformation, but they explore fundamentally different regions of the possible geometric configurations. The choice between them depends on the desired geometric properties and the physical or mathematical context of the application. These results demonstrate that the ternary fractal

transformation with $ij = -1$ successfully extends the concept of fractal Julia maps to three-dimensional chaotic systems. The transformation generates visually distinct and mathematically well-defined fractal structures that preserve the essential characteristics of the original attractor while introducing additional complexity through iterative branching. The structural multiplication reveals the underlying geometric organization of the chaotic attractor.

5.3. Fractal dimension of the transformed sets

Since the inverse-Julia transformation is a pointwise geometric remapping of the sampled attractor, it does not alter the temporal evolution of system (2.3), and a quantitative description must be defined on the point sets themselves. A natural descriptor is the box-counting dimension $\dim_B$. The following statement shows that the inverse-Julia map multiplies the structures without changing their fractal dimension.

Proposition 3. *Let $K \subset \mathbb{C}$ be compact with $0 \notin K$, and let $S_N = \{w : w^{2^N} \in K\}$. Then $\dim_B S_N = \dim_B K$ (for the upper and lower box dimensions, and also for the Hausdorff dimension), and S_N has zero two-dimensional Lebesgue measure if and only if K also does.*

Proof. It suffices to consider $N = 1$ and to iterate, since S_1 is again compact and avoids the origin. Let $0 < r_0 \le |z| \le R_0$ on K. The map $f(w) = w^2$ sends S_1 onto K and is Lipschitz on S_1 because $|w^2 - w'^2| \le 2\sqrt{R_0}\,|w - w'|$; hence $\dim_B K \le \dim_B S_1$. Conversely, write S_1 as the union of its intersections with the four closed quadrants $Q_1, \ldots, Q_4$. On each $S_1 \cap Q_j$, f is injective and its inverse is Lipschitz: for $w, w' \in Q_j$, the angle between w and w' is at most $\pi/2$, so $|w + w'| \ge \sqrt{2}\,\sqrt{r_0}$ and $|w - w'| = |w^2 - w'^2|/|w + w'| \le |w^2 - w'^2|/(\sqrt{2}\,\sqrt{r_0})$. Thus S_1 is a finite union of Lipschitz images of subsets of K, and $\dim_B S_1 \le \dim_B K$. Lipschitz maps do not increase the box or Hausdorff dimension and map sets of zero Lebesgue measure to sets of zero measure, which proves all statements. □

Table 4. Box-counting dimension estimates D_{box} of the (x_1, x_2) projection of the attractor of system (2.3) ($a = 5$, $b = 96$) and of the transformed point sets (1.5×10^5 points per set; scale window 1/16–1/256 of the normalized support; for methods A–C, mean over five random subsets, standard deviation ≤ 0.008).

Point set	D_{box}
Original (x_1, x_2) projection	1.688
Julia process, $N = 1$	1.732
Julia process, $N = 2$	1.723
Julia process, $N = 3$	1.706
Method A (Orbit cloud)	1.622
Method B (Multiscroll)	1.627
Method C (Fractal web)	1.704

The attractor projections used in Section 5 avoid the origin (for the (x_1, x_2) projection, $|z| \ge 0.53$), so Proposition 3 applies: The Julia process creates 2^N congruent copies (Proposition 1) but does not increase the fractal dimension. Table 4 reports numerical box-counting estimates obtained with the same sample size for all sets (1.5×10^5 points of the (x_1, x_2) projection on $t \in [150, 300]$, scale

window 1/16–1/256 of the normalized support); the Mandelbrot-based sets of Section 6 are included for comparison and are analyzed in Section 6.5. The estimates for the Julia process differ from that of the original attractor by at most 0.05, which is within the accuracy of box counting on a finite sample and a finite range of scales, in agreement with Proposition 3. In an earlier version of this work, a larger apparent increase of D_{box} was reported; it resulted from comparing point sets of different effective resolution and does not reflect a change of the fractal dimension.

6. Mandelbrot set-based fractal transformations: a novel approach

In this section, we apply three different transformation algorithms to the chaotic attractor projections (x_1, x_2) to generate fractal structures. The transformation methods are based on the dynamics of the Mandelbrot set and compared with the inverse Julia map approach. While inverse Julia maps explore phase space dynamics with fixed fractal parameters, an alternative strategy involves forward iteration through Mandelbrot parameter space, where chaotic sequences directly determine the complex parameter C rather than serving as initial conditions. This complementary perspective motivates the three Mandelbrot-based transformation methods introduced below. Their building blocks (the quadratic map, orbit accumulation, point reflection, and multiple seeds) are standard; to the best of our knowledge, apart from their use for pattern design in our recent work [47], their combination with parameters supplied by the trajectory of a continuous-time chaotic system has not been studied systematically before. The relation of each method to known techniques is indicated below. All three methods use the (x_1, x_2) projection of the numerical solution of system (2.3) ($a = 5$, $b = 96$, initial conditions (3.5)) computed with an adaptive fourth/fifth-order Runge–Kutta scheme (relative and absolute tolerances 10^{-8} and 10^{-10}) on $t \in [0, 300]$; the first half of the solution is discarded as transient and every tenth output point is retained, which gives $N = 9585$ points (x_i, y_i). All parameter values are listed in Algorithms 1–3 and Table 5.

Table 5. The three Mandelbrot-based methods as instances of the unified framework (6.1).

Component	**Method A (orbit cloud)**	**Method B (multiscroll)**	**Method C (fractal web)**	**Julia (Sec. 5)**
Normalization Φ	$[-0.5, 0.1] \times [0, 0.6]$	$[-0.6, -0.2] \times [-0.4, 0.4]$ (level 0 only)	$[-0.75, -0.6] \times [0, 0.25]$	— ($c \equiv 0$)
Seed set Z_0	$\{0\}$	$\{0\}$	$\{0, \pm 0.1, \pm 0.1i\}$	From trajectory
Branching $\mathcal{B}$	Identity	Quadrant reflection, depth D	Identity	Sign branching
Accumulation $\mathcal{A}$	All iterates z_k	Final iterate z_K	All iterates z_k	All iterates
Iterations N_{iter}	15 ($T_{\text{div}} = 50$)	$K = 3$ per level	12 ($T_{\text{div}} = 30$)	—

Algorithm 1: Mandelbrot orbit cloud transformation.

Input: Chaotic trajectory $\mathbf{X} = \{(x_i, y_i)\}_{i=1}^{N}$
Output: Transformed attractor $\mathbf{P} = \{(u_j, v_j)\}_{j=1}^{M}$

Parameters: $N_{\text{iter}} = 15$, $T_{\text{div}} = 50$
$\mathbf{P} \leftarrow \{\}$;
for $i = 1, 6, 11, \ldots$ *(every fifth point of* $\mathbf{X}$*)* **do**
  $c_i \leftarrow (x_i - x_{\min})/(x_{\max} - x_{\min}) \cdot 0.6 - 0.5;$
    $+ i \cdot [(y_i - y_{\min})/(y_{\max} - y_{\min}) \cdot 0.6];$
  $z \leftarrow 0 + 0i$;
  for $k = 1$ *to* N_{iter} **do**
    $z \leftarrow z^2 + c_i$;
    if $|z| > T_{div}$ **then**
      break;
    $(u, v) \leftarrow (\text{Re}(z), \text{Im}(z))$;
    $\mathbf{P} \leftarrow \mathbf{P} \cup \{(u, v)\}$;
return P

Algorithm 2: Construction of the Mandelbrot multiscroll via the quadrant reflection method.

Input: Normalized initial coordinates: $x_{\text{norm}}, y_{\text{norm}}$; depth D; number of iterations K
Output: Set of points (u, v) of the multiscroll attractor
Initialization: $u^{(0)} \leftarrow x_{\text{norm}},\ v^{(0)} \leftarrow y_{\text{norm}}$;
for $d \leftarrow 1$ **to** D **do**
  for *each point* $(u_i^{(d-1)}, v_i^{(d-1)})$ *at the current level* **do**
    $c \leftarrow u_i^{(d-1)} + i \cdot v_i^{(d-1)}$;
    $z \leftarrow 0$;
    for $k \leftarrow 1$ **to** K **do**
      $z \leftarrow z^2 + c$;
    $\text{Re}_z \leftarrow \text{Re}(z),\ \text{Im}_z \leftarrow \text{Im}(z)$;
    Add $(\text{Re}_z, \text{Im}_z)$ to $u^{(d)}, v^{(d)}$;
    Add $(-\text{Re}_z, -\text{Im}_z)$ to $u^{(d)}, v^{(d)}$;

Algorithm 3: Construction of the fractal web through multiple initial condition sampling.

Input: Normalized trajectory coordinates: $x_{\text{norm}}, y_{\text{norm}}$; number of iterations N_{iter}; set of initial conditions $Z_0 = \{0, 0.1, -0.1, 0.1i, -0.1i\}$

Output: Set of points (u, v) forming the fractal web

for *every eighth normalized trajectory point* $(x_{norm,i}, y_{norm,i})$ **do**
  $c \leftarrow x_{\text{norm},i} + i \cdot y_{\text{norm},i}$;
  for *each initial condition* $z_0 \in Z_0$ **do**
    $z \leftarrow z_0$;
    for $k \leftarrow 1$ **to** N_{iter} **do**
      $z \leftarrow z^2 + c$;
      if $|z| > 30$ **then**
        break;
      $\text{Re}_z \leftarrow \text{Re}(z),\ \text{Im}_z \leftarrow \text{Im}(z)$;
      Record point $(\text{Re}_z, \text{Im}_z)$;

6.1. Unified transformation framework

Although the three methods introduced in this section produce visually different attractors, they are instances of a single parametric operator acting on the quadratic map $z \mapsto z^2 + c$. Given the chaotic trajectory $\mathbf{X} = \{(x_i, y_i)\}_{i=1}^{N}$ obtained from the (x_1, x_2) projection of system (2.3), a Mandelbrot-based transformation is completely specified by the tuple

$$\mathcal{T} = (\Phi,\ Z_0,\ \mathcal{B},\ \mathcal{A},\ N_{\text{iter}}), \tag{6.1}$$

whose components are:

- a *normalization map* $\Phi : \mathbb{R}^2 \to \mathbb{C}$ that sends each trajectory point to a complex parameter $c_i = \Phi(x_i, y_i)$ in a prescribed region of the Mandelbrot parameter plane;
- a *seed set* $Z_0 \subset \mathbb{C}$ of initial conditions for the orbit;
- a *branching operator* $\mathcal{B}$ applied after each iteration level (the identity or a symmetric reflection);
- an *accumulation rule* $\mathcal{A}$ specifying which iterates z_k are recorded (all intermediate points, or only the final one);
- the maximum number of iterations N_{iter} (with an optional divergence threshold T_{div}).

The common iteration underlying all three methods is

$$z_0 \in Z_0, \qquad z_{k+1} = z_k^2 + c_i, \qquad k = 0, 1, \ldots, N_{\text{iter}} - 1, \tag{6.2}$$

and the transformed attractor is the accumulated point set

$$\mathbf{P} = \bigcup_{i=1}^{N} \bigcup_{z_0 \in Z_0} \mathcal{B}\Big(\mathcal{A}\big(\{z_k\}_{k=0}^{N_{\text{iter}}}\big)\Big), \qquad (u, v) = (\text{Re}\, z,\ \text{Im}\, z). \tag{6.3}$$

The three methods of this section are recovered by particular choices of the tuple (6.1), as summarized in Table 5. In this common notation, the inverse-Julia transformation of Section 5 corresponds to the complementary limit in which the parameter is fixed ($c \equiv 0$) and the chaotic trajectory instead supplies the seed z_0, so that phase space rather than parameter space is explored.

6.2. *Mandelbrot orbit cloud (Method A)*

For each point (x_i, y_i) of the chaotic trajectory, we apply the transformation procedure detailed in Algorithm 1, which normalizes coordinates to the window $c \in [-0.5, 0.1] \times [0, 0.6]$ of the Mandelbrot parameter plane and generates orbits from $z_0 = 0$. To limit the size of the output, every fifth trajectory point is used.

The choice of this normalization window is dictated by the geometry of the Mandelbrot set $M = \{c \in \mathbb{C} : z_0 = 0,\ z_{n+1} = z_n^2 + c \text{ remains bounded}\}$. The window $[-0.5, 0.1] \times [0, 0.6]$ covers the upper part of the main cardioid of M and its boundary; a direct check on a 400×400 grid shows that about 99% of the window belongs to M. For such parameters, the orbits of $z_0 = 0$ remain bounded, so the accumulated iterates form a dense cloud instead of being dominated by escaping orbits. The divergence threshold is related to the escape criterion of the quadratic map: if at some iterate $|z_n| > 2$ and $|z_n| \geq |c|$, then

$$|z_{n+1}| = |z_n^2 + c| \geq |z_n|^2 - |c| \geq |z_n|^2 - |z_n| = |z_n|(|z_n| - 1) > |z_n|, \tag{6.4}$$

so the orbit increases monotonically and diverges. Hence $|z| = 2$ is the escape radius. The threshold $T_{\text{div}} = 50$ in Algorithm 1 lies well above this radius; it only terminates orbits that have already escaped (for parameters near the boundary of M) and retains a longer portion of each pre-escape orbit for visualization. In Figure 26, only points with $|u|, |v| < 3$ are displayed.

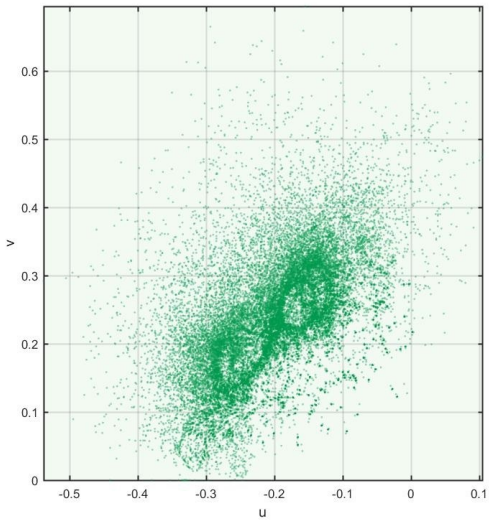


Figure 26. Mandelbrot orbit cloud transformation (Method A, $N_{\text{iter}} = 15$, $T_{\text{div}} = 50$) applied to the (x_1, x_2) projection of the attractor of system (2.3) ($a = 5$, $b = 96$).

We set the maximum iteration count to $N_{\text{iter}} = 15$ and accumulate all intermediate orbit points $(u, v) = (\text{Re}(z_k), \text{Im}(z_k))$ for $k = 1, \ldots, N_{\text{iter}}$ or until the divergence criterion $|z_k| > 50$ is satisfied. Each point of the chaotic trajectory acts as a parameter c in the Mandelbrot iteration, where the resulting attractor represents the union of orbits generated as the chaotic trajectory explores the parameter space. This approach creates a cloud-like fractal structure with interweaving patterns characterized by several distinctive features: a smooth, cloud-like morphology with continuous density gradients; multiple overlapping orbital trajectories that create a layered appearance; self-similar fractal patterns observable

at different scales; a dense central region that gradually transitions to sparse peripheral structures; and a point count of approximately $O(N \cdot N_{\text{iter}})$, where N is the length of the original trajectory and N_{iter} is the number of iterations per orbit. The visual result, shown in Figure 26, exhibits a structural feature distinct from traditional multiscroll attractors, resembling a turbulent flow field or cosmic nebula rather than the geometric patterns typical of inverse Julia map transformations. Method A is related to orbit-density visualizations of the quadratic family, such as the Buddhabrot technique [60], in which the orbits of $z \mapsto z^2 + c$, $z_0 = 0$, are accumulated for uniformly sampled parameters c outside the Mandelbrot set, and its "anti-Buddhabrot" variant, which accumulates the non-escaping orbits. Method A is closest to the latter, with two differences: the parameters c_i are supplied by the chaotic trajectory rather than sampled uniformly, so that the point density is weighted by the distribution of the attractor points in the normalized parameter plane, and all of them lie in the main cardioid, so that the accumulated orbit points converge to the conformal image $z^*(\Phi_A(K))$ of the attractor (Proposition 4).

6.3. Mandelbrot multiscroll (Method B)

This method combines Mandelbrot forward iteration with binary branching to create a controlled multiscroll pattern. The method for creating a multiscroll pattern is described in Algorithm 2.

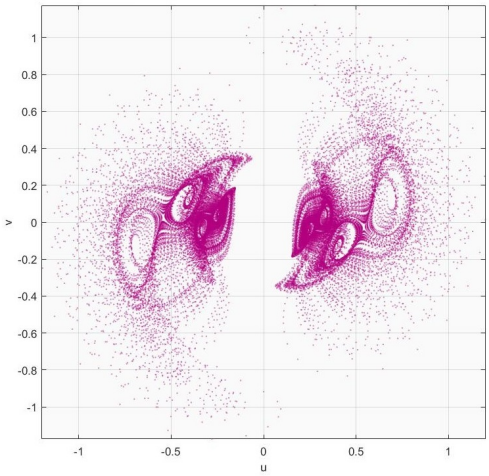


Figure 27. Mandelbrot multiscroll (Method B, depth $D = 2$, $K = 3$) applied to the (x_1, x_2) projection of the attractor of system (2.3) ($a = 5$, $b = 96$).

Let $D = 2$ be the depth and $K = 3$ the number of Mandelbrot iterations per level. The normalized input coordinates are obtained by the affine map $x_{\text{norm}} = -0.6 + 0.4\,(x_i - x_{\min})/(x_{\max} - x_{\min})$, $y_{\text{norm}} = -0.4 + 0.8\,(y_i - y_{\min})/(y_{\max} - y_{\min})$, i.e., the trajectory is mapped onto the window $[-0.6, -0.2] \times [-0.4, 0.4]$, which lies entirely inside the main cardioid of the Mandelbrot set. This normalization is applied only at level $d = 0$; at the subsequent levels, the points $(\operatorname{Re} z, \operatorname{Im} z)$ obtained at the previous level are used directly as parameter c, and only the points of the last level are retained. The branching step $(\operatorname{Re} z, \operatorname{Im} z) \mapsto (-\operatorname{Re} z, -\operatorname{Im} z)$ is the point reflection $z \mapsto -z$, which is also the symmetry exchanging the two branches of the inverse Julia map; in this sense, Method B combines forward Mandelbrot iteration with the branching mechanism of the Julia process [26]. The method iteratively expands the attractor through quadrant reflection, creating 2^D distinct scrolls. Each depth level applies forward Mandelbrot

dynamics followed by symmetric branching, analogous to the bifurcation cascade in period-doubling scenarios. The resulting structure (see Figure 27) exhibits discrete, well-separated scrolls arranged symmetrically, with $2^D = 4$ main scrolls for $D = 2$, giving a geometric, crystalline appearance and clear separation between scroll regions. The total number of points generated is $N \cdot 2^D$.

6.4. Fractal web (Method C)

This method generates a web-like structure by computing multiple orbits from different initial conditions for each parameter value as shown in Algorithm 3.

Here $N_{\text{iter}} = 12$ and normalization targets the boundary region of the Mandelbrot set near $c \approx -0.75 + 0i$ (the neck between the main cardioid and the period-2 bulb): The trajectory is mapped onto the window $[-0.75, -0.6] \times [0, 0.25]$ by $x_{\text{norm}} = -0.75 + 0.15\,(x_i - x_{\min})/(x_{\max} - x_{\min})$, $y_{\text{norm}} = 0.25\,(y_i - y_{\min})/(y_{\max} - y_{\min})$, and every eighth trajectory point is used. Orbits are terminated when $|z| > 30$. By using several seeds z_0 for each parameter value c, the method shows how orbits started from different initial points evolve under the same quadratic map; this is equivalent to superimposing short orbit segments of the corresponding Julia-set dynamics. The resulting web pattern (see Figure 28) shows how different initial conditions converge or diverge under the same parameter value. The structure exhibits an intricate, lace-like pattern resembling a spider web, with radial filaments connecting central and peripheral regions, demonstrating a high degree of interconnectivity. This reveals the topological structure of the parameter space and displays an intermediate density compared to Methods A (Mandelbrot orbit cloud) and B (Mandelbrot multiscroll).

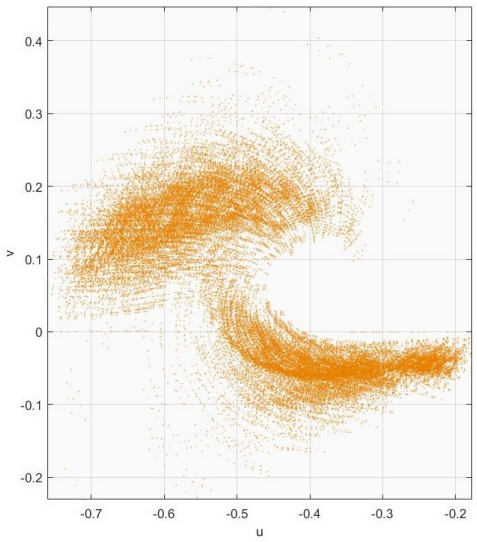


Figure 28. Fractal web (Method C, $N_{\text{iter}} = 12$, $Z_0 = \{0, \pm 0.1, \pm 0.1i\}$) applied to the (x_1, x_2) projection of the attractor of system (2.3) ($a = 5$, $b = 96$).

6.5. Convergence, dimension, and measure of the Mandelbrot-based sets

Let K denote the (x_1, x_2) projection of the attractor, identified with a compact subset of $\mathbb{C}$, and let Φ_A, Φ_B, Φ_C be the affine normalization maps of Methods A–C. Write $p_k(c) = f_c^k(0)$ and $q_{k,z_0}(c) = f_c^k(z_0)$ for $f_c(z) = z^2 + c$; these are polynomials in c (e.g., $p_1 = c$, $p_2 = c^2 + c$, $p_3 = (c^2 + c)^2 + c$). In the

absence of escapes, the generated sets are

$$P_A = \bigcup_{k=1}^{15} p_k(\Phi_A(K)), \qquad P_B = \bigcup_{\sigma_1,\sigma_2=\pm 1} \sigma_2\, p_3(\sigma_1\, p_3(\Phi_B(K))), \qquad P_C = \bigcup_{z_0\in Z_0}\bigcup_{k=1}^{12} q_{k,z_0}(\Phi_C(K)). \quad (6.5)$$

Proposition 4. *(i) Each of the sets P_A, P_B, P_C is a finite union of images of K under polynomial maps; hence* $\dim_B P \le \dim_B K$ *for each of them, and P has a zero two-dimensional Lebesgue measure whenever* $\dim_B K < 2$. *(ii) If c lies in the interior of the main cardioid $C = \{c : |1 - \sqrt{1-4c}| < 1\}$ of the Mandelbrot set, then f_c has the attracting fixed point $z^*(c) = (1 - \sqrt{1-4c})/2$ with the multiplier $\lambda(c) = 2z^*(c)$, $|\lambda(c)| < 1$, and the orbit of the critical point $z_0 = 0$ converges to $z^*(c)$ asymptotically as $|z_k - z^*(c)| \sim C|\lambda(c)|^k$. The map $c \mapsto z^*(c)$ is analytic on C with* $\mathrm{d}z^*/\mathrm{d}c = 1/\sqrt{1-4c} \neq 0$.

Proof. (i) Polynomials are Lipschitz on bounded sets and Φ_A, Φ_B, Φ_C are affine. Lipschitz maps do not increase the box dimension, the dimension of a finite union is the maximum of the dimensions, and a set with $\dim_B < 2$ has a zero Lebesgue measure. (ii) The fixed-point equation $z^2 - z + c = 0$ has the root $z^*(c)$ given above, and $f_c'(z^*) = 2z^*$; the condition $|2z^*| < 1$ is the definition of C. By Fatou's theorem, the immediate basin of an attracting fixed point contains a critical point, and the only critical point of f_c is 0; hence $f_c^k(0) \to z^*(c)$, with the linear rate given by the multiplier. The derivative of z^* follows by differentiation. □

For the normalization windows used here, all parameters supplied by the trajectory lie in C (checked for every point for Methods A and C), so every orbit converges and the divergence thresholds T_{div} are never reached; accordingly, the numbers of generated points coincide exactly with $\lceil N/5\rceil \cdot 15$ and $\lceil N/8\rceil \cdot 5 \cdot 12$, and the largest moduli are $|z| \le 0.65$ (Method A) and $|z| \le 0.76$ (Method C). Proposition 4 gives a precise description of the three structures. In Method A, $|\lambda|$ ranges from 0.15 to 0.91 (median 0.61), so the orbits approach $z^*(c)$ rapidly (median distance $\approx 10^{-4}$ after 15 iterations); the cloud consists of the transient orbit points accumulating on the set $z^*(\Phi_A(K))$, which is a conformal image of the attractor projection, and this explains the dense central region. In Method C, the window lies at the junction of the main cardioid and the period-2 bulb, where $\lambda \to -1$ (up to $|\lambda| = 0.998$): convergence is very slow and the orbit points alternate between the two sides of $z^*(c)$, which produces the two filamentary arms of the web in Figure 28. Method B involves only a fixed number of iterations ($K = 3$ per level) and is an explicit polynomial map without any convergence issue. In agreement with Proposition 4(i), the box-counting estimates for Methods A–C in Table 4 do not exceed that of the original projection. Hence none of the Mandelbrot-based methods increases the fractal dimension of the attractor; they produce new structured point sets whose dimension is bounded by that of the attractor projection and whose Lebesgue measure is zero.

6.6. Comparative analysis

Table 6 summarizes the key differences between the methods.

Table 6. Comparison of fractal transformation methods.

Feature	Method A	Method B	Method C	Julia
Mathematical basis	Forward	Hybrid	Multi-seed	Inverse
Parameter c	From trajectory	Iterative	From trajectory	Fixed (0)
Initial z_0	Fixed (0)	Fixed (0)	Multiple	From trajectory
Structure type	Cloud	Geometric	Web	Star
Number of scrolls	Continuous	2^D discrete	Filamentary	2^N discrete
Density profile	Central peak	Uniform	Filamentary	Uniform
D_{box} (Table 4)	1.62	1.63	1.70	1.71–1.73

The fundamental difference between the new Methods (A–C) and the Julia approach lies in the role of the chaotic trajectory:

- **Mandelbrot-based Methods (A–C):** The chaotic trajectory provides parameter values c, while the initial condition is fixed at $z_0 = 0$. The transformation explores the parameter space of the Mandelbrot set:

$$M = \{c \in \mathbb{C} : \lim_{n\to\infty} |z_n| < \infty, \text{ where } z_0 = 0, z_{n+1} = z_n^2 + c\}. \tag{6.6}$$

- **Julia-based method:** The chaotic trajectory provides initial conditions z_0, while the parameter is fixed at $c = 0$. The transformation explores the phase space of a specific Julia set:

$$J_0 = \{z_0 \in \mathbb{C} : \lim_{n\to\infty} |z_n| < \infty, \text{ where } z_{n+1} = z_n^2\}. \tag{6.7}$$

Exploring parameter space (Mandelbrot) versus phase space (Julia) generates fundamentally different classes of multiscroll attractors, despite both being rooted in the quadratic complex map $z \mapsto z^2 + c$.

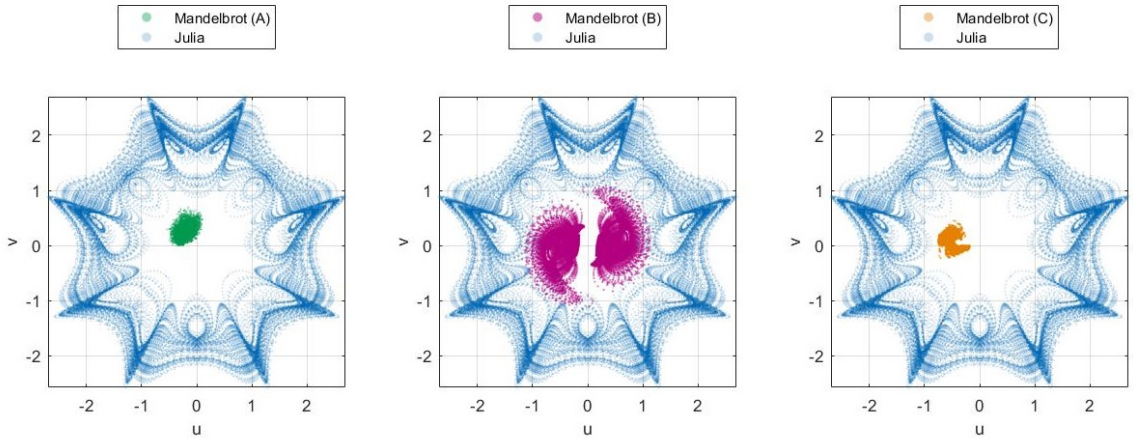


Figure 29. Comparative visualization of three Mandelbrot-based attractor generation Methods (A–C), applied to the (x_1, x_2) projection of the attractor of system (2.3) ($a = 5$, $b = 96$), alongside their corresponding Julia set counterparts. Each column presents a pair: Mandelbrot attractor (top) and its associated Julia set (bottom) for the respective parameter sampling or transformation method. This side-by-side arrangement highlights the intrinsic connection between the global parameter space structure (Mandelbrot) and the local dynamical behavior (Julia) for each algorithmic approach.

All methods successfully transform the original two-scroll chaotic attractor into complex multiscroll structures, but with markedly different topological and geometric properties (see Figure 29). The Mandelbrot-based approaches (Methods A–C) offer new degrees of freedom for designing chaotic systems with specific spatial structures, which may be advantageous for applications in secure communications and image encryption.

7. Conclusions

In this paper, we present a new four-dimensional memristive chaotic system without equilibrium points, consisting of only seven terms. A detailed dynamical analysis of the new system is performed, including the construction of bifurcation diagrams, the calculation of the Lyapunov exponents and the Kaplan–Yorke dimension, phase portraits, and the study of multistability and offset boosting. Poincaré cross-sections, power spectral analysis, NIST SP 800-22 randomness testing, and a Lyapunov-function-based analysis were employed to characterize the dynamics of the proposed system; the boundedness of the variables (x_1–x_3) was established numerically, while the undamped flux x_4 drifts slowly, and the statistical quality of the generated sequences was confirmed. The proposed model was further validated through electronic circuit implementation in the Multisim environment, confirming its physical realizability and practical feasibility.

A central contribution of this work is the systematic application of binary inverse Julia and ternary fractal algorithms to phase-space projections of the chaotic attractor. We showed that applying binary inverse Julia and ternary fractal algorithms to a chaotic attractor leads to structurally multiplied patterns that follow a power law $M_2 = M_1 \times 2^N$ in several phase space projections. We proved that after N iterations, the transformed set consists of 2^N congruent copies with exact 2^N-fold rotational symmetry, whereas the number of connected components doubles only if the projected attractor does not surround the origin. We also developed and compared two different ternary formulations ($ij = -1$ and $ij = 0$), revealing fundamentally different geometric results, ranging from anisotropic ribbon structures to isotropic concentric patterns.

Three new Mandelbrot set-based transformation methods were proposed, exploring parameter space instead of phase space and generating different classes of attractors (cloud, multiscroll, and web-like structures), complementing traditional Julia set-based approaches.

The proposed approach offers several advantages. The source system is structurally minimal, containing only seven terms and no equilibria, yet it generates hidden chaotic attractors; its physical realizability is confirmed by the Multisim circuit. The fractal-transformation framework is versatile: The inverse-Julia maps multiply the number of structural components as $M_2 = M_1 \times 2^N$ with an exact 2^N-fold rotational symmetry, while preserving the fractal dimension of the attractor projection (Proposition 3) and leaving the dynamical invariants unchanged, and the Mandelbrot-based methods add independent degrees of freedom for shaping the resulting patterns. The two ternary rules ($ij = -1$ and $ij = 0$) further provide explicit control over anisotropic versus isotropic geometries.

At the same time, the method has limitations that should be acknowledged. For this equilibrium-free system, a single global compact bound on the trajectories cannot be obtained from a quadratic Lyapunov function (Section 3.6), so boundedness rests on numerical evidence rather than a closed-form estimate. Moreover, the flux x_4 is undamped and drifts slowly, so that the memristor is saturated on the attractor; this gives rise to an additional neutral Lyapunov exponent and excludes hyperchaos

in the present model. The ternary transformation with $ij = -1$ is singular on the half-plane Σ_{-1}, near which the transformed coordinates become very large. All transformations considered here are geometric post-processing of the trajectory: They generate structured patterns but do not increase the fractal dimension of the attractor (Propositions 3 and 4) and do not change its dynamics. Finally, the present study is confined to numerical and circuit-level validation.

Future work will address these points along several directions. A rigorous ultimate-bound estimate could be sought using non-quadratic or piecewise Lyapunov functions, or by introducing weak damping into the flux channel ($\dot{x}_4 = x_2 - \varepsilon x_4$), which would also keep the memristor active on the attractor and may lead to genuine hyperchaos. The synchronization of the proposed system deserves particular attention: the fast fixed-time control of multi-layer networks [52] and the event-triggered strategies for multi-agent systems with time-varying delays [53] offer promising frameworks for master–slave synchronization, which is a prerequisite for chaos-based secure communication. Further directions include hardware realization on Field-Programmable Gate Array (FPGA)/Digital Signal Processor (DSP) platforms, quantitative evaluation of the fractal-transformed sequences in image-encryption pipelines, and extension of the ternary and Mandelbrot frameworks to higher-dimensional and fractional-order memristive systems.

These findings show that fractal transformations are a versatile tool for generating complex, structurally controlled patterns from memristive chaotic systems. Possible applications, for example, in pattern generation [47] or in chaos-based encryption, would require dedicated algorithm design, and performance and security analysis, which is beyond the scope of the present work.

Author contributions

M.I. Kopp: Conceptualization, methodology, software, validation, formal analysis, investigation, data curation, writing–original draft preparation, writing–review and editing, visualization, supervision; I. Samuilik: Conceptualization, validation, investigation, resources, writing–review and editing, visualization, supervision. Both authors have read and approved the final version of the manuscript for publication.

Use of Generative-AI tools declaration

The authors declare they have not used Artificial Intelligence (AI) tools in the creation of this article.

Acknowledgments

The authors are grateful to all six reviewers for their valuable comments, which significantly improved the manuscript.

Conflict of interest

The authors declare no conflicts of interest.

References

1. B. B. Mandelbrot, *The fractal geometry of nature*, New York: W. H. Freeman, 1982.
2. H. O. Peitgen, H. Jürgens, D. Saupe, *Chaos and fractals: new frontiers of science*, 2 Eds., New York: Springer, 2004. https://doi.org/10.1007/b97624
3. J. C. Sprott, *Chaos and time-series analysis*, Oxford: Oxford University Press, 2003.
4. L. O. Chua, Memristor—The missing circuit element, *IEEE Trans. Circuit Theory*, **18** (1971), 507–519. https://doi.org/10.1109/TCT.1971.1083337
5. D. B. Strukov, G. S. Snider, D. R. Stewart, R. S. Williams, The missing memristor found, *Nature*, **453** (2008), 80–83. https://doi.org/10.1038/nature06932
6. Z. Wei, Dynamical behaviors of a chaotic system with no equilibria, *Phys. Lett. A*, **376** (2011), 102–108. https://doi.org/10.1016/j.physleta.2011.10.040
7. V. T. Pham, C. Volos, S. Vaidyanathan, T. P. Le, V. Y. Vu, A memristor-based hyperchaotic system with hidden attractors: dynamics, synchronization and circuital emulating, *J. Eng. Sci. Technol. Rev.*, **8** (2015), 205–214. https://doi.org/10.25103/jestr.082.26
8. K. Rajagopal, V. T. Pham, F. R. Tahir, A. Akgul, H. R. Abdolmohammadi, S. Jafari, A chaotic jerk system with non-hyperbolic equilibrium: Dynamics, effect of time delay and circuit realization, *Pramana*, **90** (2018), 52. https://doi.org/10.1007/s12043-018-1545-x
9. X. C. Liu, Q. Tu, Coexisting and hidden attractors of memristive chaotic systems with and without equilibria, *Eur. Phys. J. Plus*, **137** (2022), 516. https://doi.org/10.1140/epjp/s13360-022-02720-9
10. A. Bayani, K. Rajagopal, A. J. M. Khalaf, S. Jafari, G. D. Leutcho, J. Kengne, Dynamical analysis of a new multistable chaotic system with hidden attractor: antimonotonicity, coexisting multiple attractors, and offset boosting, *Phys. Lett. A*, **383** (2019), 1450–1456. https://doi.org/10.1016/j.physleta.2019.02.005
11. S. Gu, Q. Peng, X. Leng, B. Du, A novel non-equilibrium memristor-based system with multi-wing attractors and multiple transient transitions, *Chaos*, **31** (2021), 033105. https://doi.org/10.1063/5.0039121
12. M. I. Kopp, Chaos and complexity in a four-dimensional system with hyperbolic tangent nonlinearity and no equilibrium, *TWMS J. Appl. Eng. Math.*, **15** (2025), 2584–2598.
13. M. Kopp, Dynamical analysis, circuit design, and synchronization of a new 4D two-wing memristor-based hyperchaotic system with no equilibrium, *TechRxiv*, 2024. https://doi.org/10.36227/techrxiv.172548128.82541253/v1
14. M. I. Kopp, A new memristor-based 4D hyperchaotic system with seven terms and no equilibrium points, *Nonlinear Dyn. Syst. Theory*, **25** (2025), 288–298.
15. M. I. Kopp, I. Samuilik, Hidden attractors in a new 4D memristor-based hyperchaotic system: dynamical analysis, circuit design, synchronization, and its applications, *Mathematics*, **13** (2025), 2838. https://doi.org/10.3390/math13172838
16. H. Jahanshahi, O. Orozco-López, J. M. Munoz-Pacheco, N. D. Alotaibi, C. Volos, Z. Wang, et al., Simulation and experimental validation of a non-equilibrium chaotic system, *Chaos Soliton. Fract.*, **143** (2021), 110539. https://doi.org/10.1016/j.chaos.2020.110539

17. Y. Li, C. Dong, H. Li, Design, dynamic analysis, and application of a novel four-dimensional memristor-based chaotic system with hidden attractors, *Phys. Scr.*, **100** (2025), 045231. https://doi.org/10.1088/1402-4896/adbd8a

18. Q. Wang, H. Sang, P. Wang, X. Yu, Z. Yang, A novel 4D chaotic system coupling with dual-memristors and application in image encryption, *Sci. Rep.*, **14** (2024), 29615. https://doi.org/10.1038/s41598-024-80445-8

19. Q. Lai, Z. Wan, L. K. Kengne, P. D. K. Kuate, C. Chen, Two-memristor-based chaotic system with infinite coexisting attractors, *IEEE Trans. Circuits Syst. II*, **68** (2021), 2197–2201. https://doi.org/10.1109/TCSII.2020.3044096

20. S. Zhang, J. Zheng, X. Wang, Z. Zeng, Multi-scroll hidden attractor in memristive HR neuron model under electromagnetic radiation and its applications, *Chaos*, **31** (2021), 011101. https://doi.org/10.1063/5.0035595

21. V. T. Pham, S. Jafari, S. Vaidyanathan, C. Volos, X. Wang, A novel memristive neural network with hidden attractors and its circuitry implementation, *Sci. China Technol. Sci.*, **59** (2016), 358–363. https://doi.org/10.1007/s11431-015-5981-2

22. Z. Wan, Y. F. Pu, Q. Lai, Multiscroll hidden attractor in memristive autapse neuron model and its memristor-based scroll control and application in image encryption, *Neural Networks*, **188** (2025), 107473. https://doi.org/10.1016/j.neunet.2025.107473

23. Z. Wan, Y. F. Pu, M. Qin, Q. Lai, Robust full-parameter control method: Constructing multiscroll HNN via memristor, *Neural Networks*, **192** (2025), 107878. https://doi.org/10.1016/j.neunet.2025.107878

24. Z. Wan, Y. F. Pu, Y. Liu, Q. Lai, Z. Yang, State-based nonlinear mapping method for constructing conservative oscillator generating cellular chaotic sea with hardware implementation, *Chaos Soliton. Fract.*, **211** (2026), 118789. https://doi.org/10.1016/j.chaos.2026.118789

25. G. Julia, Mémoire sur l'itération des fonctions rationnelles, *J. Math. Pures Appl.*, **1** (1918), 47–245.

26. K. Bouallegue, A. Chaari, A. Toumi, Multi-scroll and multi-wing chaotic attractor generated with Julia process fractal, *Chaos Soliton. Fract.*, **44** (2011), 79–85. https://doi.org/10.1016/j.chaos.2010.12.005

27. K. Bouallegue, A new fractal model of chromosome and DNA processes, In: S. Stavrinides, S. Banerjee, S. Caglar, M. Ozer, *Chaos and complex systems*, Berlin, Heidelberg: Springer, 2013, 505–514. https://doi.org/10.1007/978-3-642-33914-1_71

28. K. Bouallegue, Gallery of chaotic attractors generated by fractal network, *Int. J. Bifurcat. Chaos*, **25** (2015), 1530002. https://doi.org/10.1142/S0218127415300025

29. S. Dai, K. Sun, S. He, W. Ai, Complex chaotic attractor via fractal transformation, *Entropy*, **21** (2019), 1115. https://doi.org/10.3390/e21111115

30. X. Wang, L. Feng, H. Zhao, Fast image encryption algorithm based on parallel computing system, *Inf. Sci.*, **486** (2019), 340–358. https://doi.org/10.1016/j.ins.2019.02.049

31. S. Zhou, X. Wang, Y. Zhang, B. Ge, M. Wang, S. Gao, A novel image encryption cryptosystem based on true random numbers and chaotic systems, *Multimedia Syst.*, **28** (2022), 95–112. https://doi.org/10.1007/s00530-021-00803-8

32. H. Liu, A. Kadir, C. Xu, Color image encryption with cipher feedback and coupling chaotic map, *Int. J. Bifurcat. Chaos*, **30** (2020), 2050173. https://doi.org/10.1142/S0218127420501734
33. Y. Zhang, The unified image encryption algorithm based on chaos and cubic S-Box, *Inf. Sci.*, **450** (2018), 361–377. https://doi.org/10.1016/j.ins.2018.03.055
34. K. H. Sun, S. B. He, Y. He, L. Z. Yin, Complexity analysis of chaotic pseudo-random sequences based on spectral entropy algorithm, *Acta Phys. Sin.*, **62** (2013), 010501. https://doi.org/10.7498/aps.62.010501
35. M. Kaur, V. Kumar, A comprehensive review on image encryption techniques, *Arch. Comput. Methods Eng.*, **27** (2020), 15–43. https://doi.org/10.1007/s11831-018-9298-8
36. M. W. Tian, S. R. Yan, X. X. Tian, S. Nojavan, K. Jermsittiparsert, Risk and profit-based bidding and offering strategies for pumped hydro storage in the energy market, *J. Clean. Prod.*, **256** (2020), 120715. https://doi.org/10.1016/j.jclepro.2020.120715
37. F. Masood, J. Ahmad, S. A. Shah, S. S. Jamal, I. Hussain, A novel hybrid secure image encryption based on Julia set of fractals and 3D Lorenz chaotic map, *Entropy*, **22** (2020), 274. https://doi.org/10.3390/e22030274
38. S. Agarwal, Secure image transmission using fractal and 2D-chaotic map, *J. Imaging*, **4** (2018), 17. https://doi.org/10.3390/jimaging4010017
39. M. Khan, F. Masood, A. Alghafis, Secure image encryption scheme based on fractals key with Fibonacci series and discrete dynamical system, *Neural Comput. Appl.*, **32** (2020), 11837–11857. https://doi.org/10.1007/s00521-019-04667-y
40. Y. Sun, R. Xu, L. Chen, X. Hu, Image compression and encryption scheme using fractal dictionary and Julia set, *IET Image Process.*, **9** (2015), 173–183. https://doi.org/10.1049/iet-ipr.2014.0224
41. Y. Zhang, X. Guo, Control of Julia sets of the complex Hénon system, *Nonlinear Dyn.*, **69** (2012), 185–192. https://doi.org/10.1007/s11071-011-0256-3
42. D. Wang, S. Liu, K. Liu, Y. Zhao, Control and synchronization of Julia sets generated by a class of complex time-delay rational map, *J. Appl. Anal. Comput.*, **6** (2016), 1049–1063. https://doi.org/10.11948/2016068
43. A. A. Elsadany, A. Aldurayhim, H. N. Agiza, A. Elsonbaty, On the fractional-order complex cosine map: fractal analysis, Julia set control and synchronization, *Mathematics*, **11** (2023), 727. https://doi.org/10.3390/math11030727
44. M. F. Danca, M. Fečkan, Mandelbrot set and Julia sets of fractional order, *Nonlinear Dyn.*, **111** (2023), 9555–9570. https://doi.org/10.1007/s11071-023-08311-2
45. Y. Wang, X. Li, D. Wang, S. Liu, A brief note on fractal dynamics of fractional Mandelbrot sets, *Appl. Math. Comput.*, **432** (2022), 127353. https://doi.org/10.1016/j.amc.2022.127353
46. M. F. Danca, Mandelbrot set as a particular Julia set of fractional order, equipotential lines and external rays of Mandelbrot and Julia sets of fractional order, *Fractal Fract.*, **8** (2024), 69. https://doi.org/10.3390/fractalfract8010069
47. M. Kopp, I. Samuilik, Generation of new batik floral patterns via chaotic modulation and Julia–Mandelbrot fractal transformations, *Front. Appl. Math. Stat.*, **12** (2026), 1826475. https://doi.org/10.3389/fams.2026.1826475

48. B. Munmuangsaen, B. Srisuchinwong, A new five-term simple chaotic attractor, *Phys. Lett. A*, **373** (2009), 4038–4043. https://doi.org/10.1016/j.physleta.2009.08.068

49. G. A. Leonov, N. V. Kuznetsov, Hidden attractors in dynamical systems: From hidden oscillations in Hilbert–Kolmogorov, Aizerman, and Kalman problems to hidden chaotic attractor in Chua circuits, *Int. J. Bifurcat. Chaos*, **23** (2013), 1330002. https://doi.org/10.1142/S0218127413300024

50. G. Benettin, L. Galgani, A. Giorgilli, J. M. Strelcyn, Lyapunov characteristic exponents for smooth dynamical systems and for Hamiltonian systems; a method for computing all of them. Part 1: theory, *Meccanica*, **15** (1980), 9–20. https://doi.org/10.1007/BF02128236

51. A. Wolf, J. B. Swift, H. L. Swinney, J. A. Vastano, Determining Lyapunov exponents from a time series, *Physica D*, **16** (1985), 285–317. https://doi.org/10.1016/0167-2789(85)90011-9

52. S. Yang, H. He, M. F. Leung, Y. Tang, L. Yan, Fast fixed-time control for intra- and inter-layer synchronization of multi-layer networks, *Axioms*, **14** (2025), 795. https://doi.org/10.3390/axioms14110795

53. C. Yi, J. Li, J. Cai, Z. You, C. Jing, Event-triggered synchronization for multi-agent networked systems with time-varying coupling strength and non-differentiable delays, *Math. Comput. Simulat.*, **236** (2025), 12–28. https://doi.org/10.1016/j.matcom.2025.03.029

54. J. Wen, Y. Feng, X. Tao, Y. Cao, Dynamical analysis of a new chaotic system: hidden attractor, coexisting-attractors, offset boosting, and DSP realization, *IEEE Access*, **9** (2021), 167920–167927. https://doi.org/10.1109/ACCESS.2021.3136249

55. F. Pareschi, R. Rovatti, G. Setti, On statistical tests for randomness included in the NIST SP800-22 test suite and based on the binomial distribution, *IEEE T. Inf. Forensics Secur.*, **7** (2012), 491–505. https://doi.org/10.1109/TIFS.2012.2185227

56. Q. Deng, C. Wang, H. Lin, Memristive Hopfield neural network dynamics with heterogeneous activation functions and its application, *Chaos Soliton. Fract.*, **178** (2024), 114387. https://doi.org/10.1016/j.chaos.2023.114387

57. N. Wang, M. Cui, M. Marwan, Y. Yang, H. Bao, H. H. C. Iu, et al., Automatic design of multi-fold hyperchaotic system using parallel fractal algorithm, *IEEE Trans. Circuits Syst. II*, **72** (2025), 1313–1317. https://doi.org/10.1109/TCSII.2025.3594405

58. Y. Yang, J. Yang, C. Chen, M. Marwan, Generating multistructure attractor via modified fractal with nonautonomous switching and chaotic path planning application, *AEU-Int. J. Electron. C.*, **211** (2026), 156331. https://doi.org/10.1016/j.aeue.2026.156331

59. X. Du, L. Wang, D. Yan, S. Duan, A multiring Julia fractal chaotic system with separated-scroll attractors, *IEEE Trans. VLSI Syst.*, **29** (2021), 2210–2219. https://doi.org/10.1109/TVLSI.2021.3106312

60. M. Green, *The Buddhabrot technique*, 1993. Available from: `https://superliminal.com/fractals/bbrot/`.



AIMS Press

© 2026 the Author(s), licensee AIMS Press. This is an open access article distributed under the terms of the Creative Commons Attribution License (https://creativecommons.org/licenses/by/4.0)